

Manuscript version: Author's Accepted Manuscript

The version presented in WRAP is the author's accepted manuscript and may differ from the published version or Version of Record.

Persistent WRAP URL:

<http://wrap.warwick.ac.uk/116654>

How to cite:

Please refer to published version for the most recent bibliographic citation information. If a published version is known of, the repository item page linked to above, will contain details on accessing it.

Copyright and reuse:

The Warwick Research Archive Portal (WRAP) makes this work by researchers of the University of Warwick available open access under the following conditions.

Copyright © and all moral rights to the version of the paper presented here belong to the individual author(s) and/or other copyright owners. To the extent reasonable and practicable the material made available in WRAP has been checked for eligibility before being made available.

Copies of full items can be used for personal research or study, educational, or not-for-profit purposes without prior permission or charge. Provided that the authors, title and full bibliographic details are credited, a hyperlink and/or URL is given for the original metadata page and the content is not changed in any way.

Publisher's statement:

Please refer to the repository item page, publisher's statement section, for further information.

For more information, please contact the WRAP Team at: wrap@warwick.ac.uk.

Heteronuclear d-d and d-f Ru(II)/M complexes [M = Gd(III), Yb(III), Nd(III), Zn(II) or Mn(II)] of ligands combining phenanthroline and aminocarboxylate binding sites: combined relaxivity, cell imaging and photophysical studies.

Bethany J. Crowston,^a James D. Shipp,^a Dimitri Chekulaev,^a Luke K. McKenzie,^{a,b}

Callum Jones,^{a,b} Julia A. Weinstein,^a Anthony J. H. Meijer,^a Helen E. Bryant,^b

Louise Natrajan,^c Adam Woodward,^c and Michael D. Ward^{a,d,*}

a Department of Chemistry, University of Sheffield, Sheffield S3 7HF, UK

b Sheffield Institute for Nucleic Acids (SInFoNiA), Department of Oncology, Medical School, Beech Hill Road, Sheffield S10 2RX, UK

c Department of Chemistry, University of Manchester, Oxford Road, Manchester M13 9PL, UK

d Department of Chemistry, University of Warwick, Coventry CV4 7AL, UK. Email: m.d.ward@warwick.ac.uk

Abstract

A ligand skeleton combining a 1,10-phenanthroline (phen) binding site and one or two heptadentate N_3O_4 aminocarboxylate binding sites, connected *via* alkyne spacers to the phen C^3 or C^3/C^8 positions, has been used to prepare a range of heteronuclear **Ru•M** and **Ru•M₂** complexes which have been evaluated for their cell imaging, relaxivity, and photophysical properties. In all cases the phen unit is bound to a $\{Ru(bipy)_2\}^{2+}$ unit to give a phosphorescent $\{Ru(bipy)_2(phen)\}^{2+}$ luminophore, and the pendant aminocarboxylate sites are occupied by a secondary metal ion **M** which is either lanthanide [Gd(III), Nd(III), Yb(III)] or another d-block ion [Zn(II), Mn(II)]. When **M** = Gd(III) or Mn(II) these ions provide the complexes with a high relaxivity for water; in the case of **Ru•Gd** and **Ru•Gd₂** the combination of high water relaxivity and ³MLCT phosphorescence from the Ru(II) unit provide the possibility of two different types of imaging modality in a single molecular probe. In the case of **Ru•Mn** and **Ru•Mn₂** the Ru(II)-based phosphorescence is substantially reduced compared to the control complexes **Ru•Zn** and **Ru•Zn₂** due to the quenching effect of the Mn(II) centres. Ultrafast transient absorption spectroscopy studies on **Ru•Mn** (and **Ru•Zn** as a non-quenched control) reveal the occurrence of fast (< 1 ns) PET in **Ru•Mn**, from the Mn(II) ion to the Ru(II)-based ³MLCT state, *i.e.* $Mn^{II}-(phen^{\bullet-})-Ru^{III} \rightarrow Mn^{III}-(phen^{\bullet-})-Ru^{II}$; the resulting $Mn^{III}-(phen^{\bullet-})$ state decays with $\tau \approx 5$ ns and is non-luminescent. This occurs in conformers when an ET pathway is facilitated by a planar, conjugated bridging ligand conformation connecting the two units across the alkyne bridge but does not occur in conformers where the two units are electronically decoupled by a twisted conformation of the bridging ligand. Computational studies (DFT) on **Ru•Mn** confirmed both the occurrence of the PET quenching pathway and its dependence on molecular conformation. In the complexes **Ru•Ln** and **Ru•Ln₂** (Ln = Nd, Yb), sensitised near-infrared luminescence from Nd(III) or Yb(III) is observed following photoinduced energy-transfer from the Ru(II) core, with Ru→Nd energy-transfer being faster than Ru→Yb energy-transfer due to the higher density of energy-accepting states on Nd(III).

Introduction

The combination of transition metal and lanthanide ions in a single molecular complex (d/f complexes) has provided interesting opportunities arising from the combination of metal centres with substantially different structural, photophysical and magnetic properties.¹⁻⁴ Particular properties of d/f complexes that have attracted interest are the ability to combine blue [from Ir(III)] and red [from Eu(III)] luminescence to generate white light;² fundamental studies of d→f photoinduced energy-transfer (PEnT) including the use of d-block chromophores to act as antenna for sensitisation of near-IR lanthanide luminescence;³ and the combination of a luminescent d-block unit with a highly paramagnetic lanthanide, usually Gd(III), for preparation of dual-modal imaging agents which permit both luminescence-based visualisation of cells and magnetic resonance imaging based analysis on a larger length scale using a single probe molecule.⁴

We have recently investigated d/f complexes based on ligand skeletons combining a diimine-type unit [based on 2,2'-bipyridyl (bipy) or 1,10-phenanthroline (phen)] coordinated to a d-block centre to enable absorbance in the visible range due to metal-to-ligand charge-transfer transitions, with a polyaminocarboxylate unit that provides high kinetic and thermodynamic stability when complexed to lanthanide(III) ions.^{5,6} These Ir/Ln complexes (Scheme 1) demonstrated the ability to combine effective luminescence imaging of HeLa and MCF7 cells, including two-photon phosphorescence lifetime imaging of local O₂ concentration, with high relaxivity for the Gd(III) units associated with the rigidity of the assembly which comes from the ligand design.⁶ However, there were clearly solubility limitations arising from the hydrophobicity of the central Ir(III) core which carries a charge of only +1.

In this paper we develop the work using this ligand system in two new directions. Firstly we have used a Ru(II) *tris*-diimine unit as the d-block luminophore, given its excellent promise as a component of water-soluble, non-toxic agents for optical microscopy,⁷ and its higher charge compared to the cyclometallated Ir(III) centre (+2 vs. +1) which should aid water solubility. We have combined this with a range of lanthanide ions including Gd(III) (for its relaxivity properties) and Yb(III)/Nd(III) (for the possibility of sensitised near-IR luminescence). Secondly, we have used the pendant heptadentate polyaminocarboxylate unit as a ligand for complexing additional transition metal ions as well as just lanthanide(III) ions – creating the possibility to form d/d as well as d/f assemblies, in which ultrafast

spectroscopy studies have been used to investigate intramolecular photoinduced electron transfer from Mn(II) to the Ru-based ³MLCT state in the Ru/Mn dyad.

Results and Discussion

(i) Synthesis and characterisation.

Mononuclear Ru(II) complexes.

The synthetic strategy is summarised in Schemes 2 – 4 and is similar to the approach we used for the previously-reported Ir/Ln complexes⁶ except that the key Sonogashira coupling step, connecting the polyaminocarboxylate and phenanthroline units, was performed with the phenanthroline unit already coordinated to the Ru(II) ion: this type of ‘chemistry on the complex’ approach has been used by others.⁸ We found that the coupling worked better if we exchanged the positions of the relevant functional groups from those used previously,⁶ such that the reactive Br substituent is attached to the Ru(II) complex core as a 3-Br-phen or 3,8-Br₂-phen ligand, and the terminal alkyne is pendant from the protected polyaminocarboxylate unit.

The complex [Ru(bipy)₂(Br-phen)](PF₆)₂, **A** (Scheme 2),^{8a} was prepared by reaction of 3-Br-phen⁹ with [Ru(bipy)₂Cl₂]•2H₂O. The alkyne-containing coupling partner compound **C** (Scheme 3) required a five-step synthesis, some of these being in the literature. At first, commercially available 4-hydroxy-2,6-dimethylpyridine was brominated at the 4-position using PBr₅.¹⁰ The two methyl groups were then converted to –CH₂Br groups using radical bromination with *N*-bromosuccinimide to give 4-bromo-2,6-bis(bromomethyl)pyridine.¹¹ Installation of the *tert*-butyl protected pendant arms of the metal chelating fragments to give the known intermediate **B**¹² was achieved through a substitution reaction with two equivalents of di-(*tert*-butyl)-iminodiacetate, and then a straightforward Sonogashira reaction with trimethylsilylacetylene (TMSA) introduced the trimethylsilyl-protected alkyne group at the 4-position of the pyridine ring (compound **C**^{Si}, Scheme 3). Deprotection of the trimethylsilyl group to reveal the free alkyne **C** was carried out in THF using tetra-*n*-butylammonium fluoride (TBAF), but as this deprotection was performed *in situ* before immediate further reaction of compound **C**, no characterisation data were recorded for this

intermediate species; attempts to isolate analytically pure **C** were unsuccessful and tended to afford the Glaser-coupled di-alkyne bridged dimer.

Components **A** and **C** were then combined using a Sonogashira coupling using Cu(I) / Pd(dppf)Cl₂ as catalyst in anhydrous DMF / diisopropylamine (5:1, v/v) as solvent under argon, affording the protected Ru(II) complex **Ru•E** in 50 % yield (Scheme 2; 'E' indicates the presence of the ester protecting groups at the secondary binding site). Satisfactory characterisation was provided by ¹H NMR spectroscopy and high-resolution electrospray mass spectrometry (SI, Figs. S1 and S2). In particular at lower chemical shifts in the ¹H NMR spectrum there are singlet peaks at 1.45 ppm, 3.49 ppm and 4.00 ppm integrating as 36, 8 and 4 protons, respectively, which represent the aliphatic protons on the pendant arms of the protected secondary binding site formed from the two imino-diacetate units. Finally, removal of the *tert*-butyl protecting groups was effected by prolonged stirring of **Ru•E** with excess trifluoroacetic acid in CH₂Cl₂ to afford **Ru•L** (where 'L' denotes the deprotected secondary ligand site). Again, satisfactory characterisation was provided by ¹H NMR spectroscopy and a high-resolution ES mass spectrum (SI, Figs. S3 and S4), with the ¹H NMR spectrum confirming complete loss of the protons from the ^tBu groups (previously at 1.45 ppm). A 500 MHz COSY spectrum was used to confirm the ¹H NMR assignments.

A similar method was used to prepare the scaffold for the potentially trinuclear complexes in which there are two identical aminocarboxylate binding sites pendant from the phen ligand on the central Ru(II) unit (Scheme 4). In this case the Ru(II)-based starting complex [Ru(bipy)₂(Br₂-phen)](PF₆)₂ (complex **D**) has Br substituents at both positions C³ and C⁸ of the phen ligand. Sonogashira coupling of **D** with two equivalents of **C**, under similar conditions to those described above but with a longer reaction time, afforded complex **Ru•E₂** – with two ester-protected heptadentate binding sites on either side of the phen ligand – in 45 % yield (SI, Fig S5 and S6). The higher (twofold) symmetry compared to **Ru•E** affords a simpler ¹H NMR spectrum with the aliphatic signals arising from the protected polyaminocarboxylate arms at 1.45 ppm, 3.49 ppm and 3.99 ppm (Fig. S5) having integrals consistent with the expected 72:16:8 ratio of protons. Removal of the ester groups using the same method as described above (TFA in CH₂Cl₂) afforded the deprotected complex ligand **Ru•L₂** with two pendant binding sites. The ¹H NMR spectrum of this compound in D₂O (SI, Fig. S7) was noticeably broader and less well defined than the protected form **Ru•E₂** possibly due to a combination of the size of the complex, the viscosity

of the solvent, and strong hydrogen-bonding interactions between solute and solvent which results in slow tumbling in solution. The number of signals and their relative integrals are correct, and a high-resolution ES mass spectrum (SI, Fig. S8) confirms formulation of the complex.

*Heteronuclear **Ru•Ln** and **Ru•Ln₂** complexes (Ln = Gd, Nd, Yb).*

There are two particular reasons for studying Ru(II)/Ln(III) ('Ln' = a generic lanthanide) complexes based on this ligand skeleton. The first is that incorporation of Gd(III) ions allows preparation of potential dual-modal imaging agents based on the combination of luminescence plus magnetic resonance imaging with the same probe.^{4,6} The second is that incorporation of the near-IR emitting lanthanide ions Nd(III) and Yb(III) allows the study of sensitised emission arising from d→f PEnT.³ In both cases the fully conjugated, unsaturated structure of the bridging ligand facilitates the desired use; the structural rigidity will help to minimise the rotational correlation time of the Gd(III) centres which contributes to high relaxivity,¹³ and the electronic conjugated pathway directly connecting both Ru(II) and Ln(III) centres will facilitate Dexter-type PEnT which requires through-bond electronic coupling.⁶ The varying sizes of the lanthanide ions used mean that the heptadentate ligand will be supplemented by most likely 1 or 2 water molecules depending on ionic radius.

Dinuclear **Ru•Gd** was prepared in 84% yield simply by stirring 1.1 equivalents of GdCl₃•6H₂O with **Ru•L** in water (pH 5 – 6) for 18 h. Size-exclusion chromatography on Sephadex LH-20 in MeOH, followed by anion metathesis using Dowex 1x2 chloride resin to ensure that all hexafluorophosphate anions (from the starting Ru(II) complex) were replaced by chloride, afforded pure **Ru•Gd** as its mono-chloride salt. Trinuclear **Ru•Gd₂** was prepared similarly in 69 % yield from **Ru•L₂** and 2.6 equivalents of GdCl₃•6H₂O in aqueous solution. The complex **Ru•Gd₂** is neutral so no anion-exchange step was necessary, but was likewise purified using Sephadex LH-20 eluting with MeOH. Given that routine characterisation by ¹H NMR spectroscopy was not feasible for these complexes due to extensive paramagnetic line-broadening by the Gd(III) ions, we rely on a combination of chromatographic purity and high-resolution mass spectra (SI, Fig. S9 and S10), which for both complexes give excellent agreement with expected values as well as the correct isotopic patterns.

The heteronuclear complexes **Ru•Nd**, **Ru•Nd₂**, **Ru•Yb** and **Ru•Yb₂** were synthesised in high yields in the same manner as the analogous Ru/Gd complexes, by reaction of the

starting 'complex ligands' **Ru•L** and **Ru•L₂** with excess (1.6 equivalents or 2.8 equivalents, respectively) of the appropriate lanthanide triflate salt in water at pH 5 – 6. The dinuclear complexes **Ru•Nd** and **Ru•Yb** were anion-exchanged to the chloride salts using Dowex® 1x2 chloride ion-exchange resin and finally purified by size-exclusion chromatography on Sephadex® G-15 in water. The trinuclear complexes **Ru•Nd₂** and **Ru•Yb₂** are neutral so required no ion-exchange. As with the Ru/Gd complexes, high resolution ES mass spectrometry of these paramagnetic complexes confirmed their formulation (SI, Figs S11 – S14).

*Heteronuclear **Ru•M** and **Ru•M₂** complexes (M = Mn, Zn).*

Having used Gd(III) ions to prepare **Ru•Gd** and **Ru•Gd₂** as described above, we were interested to try other highly paramagnetic ions in these sites for possible alternative dual-modal imaging agents. Recently, interest in utilising high-spin Mn(II) ions as alternative paramagnetic centres to Gd(III) in T₁-weighted MRI contrast agents has grown,^{14,15} due to increasing concern for the *in vivo* toxicity of free Gd(III) ions. New ligand structures are beginning to be explored to incorporate Mn(II) into probes used for MR imaging purposes.¹⁴ However, examples of dual-modal luminescence/MRI probes containing Mn(II) as the paramagnetic centres are rare, with only one recent example of MnO₂ nanosheets combined with [Ru(bipy)₃](PF₆)₂ units being reported.¹⁵ Accordingly our ligand skeletons were also used to prepare Ru(II)/Mn(II) complexes to examine their luminescence and magnetic relaxivity properties; the analogous Ru(II)/Zn(II) complexes were also prepared for control experiments.

Dinuclear complexes **Ru•Mn** and **Ru•Zn** were prepared by reaction of **Ru•L** with 1.3 – 1.6 equivalents of the appropriate M(II) chloride hydrate (M = Mn, Zn) for 18 h in water at pH 5 – 6. The excess metal salt was removed by size-exclusion chromatography on Sephadex® G-15 in water to produce the pure, neutral compounds in good yields (80-95 %). As Zn(II) is diamagnetic, the successful synthesis and isolation of pure **Ru•Zn** was confirmed by ¹H NMR spectroscopy (SI, Fig. S15). The signals in the aromatic region of the ¹H NMR spectrum (400 MHz, D₂O) integrate to the expected twenty-five protons, although there are four singlets at δ = 7.52 ppm, 7.54 ppm, 8.76 ppm and 8.79 ppm that each integrate to half a proton. A two-dimensional ¹H-¹H NMR correlation spectrum confirmed that these peaks correspond to either a pyridyl H³/H⁵ pyridine proton (δ = 7.52 ppm and 7.54 ppm) and the

H² phenanthroline proton (δ = 8.76 ppm and 8.79 ppm). These half-integral values suggest the presence of two isomers in solution, which were not present in the ¹H NMR spectrum (*d*₆-DMSO, 500 MHz) of the starting complex **Ru•L**. As the protons in question are only split into inequivalent ‘halves’ in **Ru•Zn**, it would suggest that the two isomers are brought about by the chelation of the Zn(II) ion at the polyaminocarboxylate binding site to generate a chiral centre, and are therefore diastereoisomers arising from the presence of two chiral centres close together – the other chiral centre being of course the Ru(II) tris-chelate unit. This suggestion is supported by the appearance of a multiplet at δ = 3.34-3.52 ppm in the ¹H NMR spectrum for **Ru•Zn**, which integrates as eight protons, and represents the four CH₂ groups adjacent to the carboxylate groups of the secondary metal chelate site. In the ¹H NMR spectrum of **Ru•L** these 8 protons are equivalent, occurring as a singlet at δ = 3.94 ppm. However, once the Zn(II) ion is bound in **Ru•Zn**, they become inequivalent and appear as a multiplet due to the presence of the diastereoisomers. The remaining signal in the aliphatic region of the ¹H NMR spectrum is from the two CH₂ groups attached to C² and C⁶ of the pyridine ring (δ = 4.15 ppm). We could not obtain meaningful ¹H NMR spectra for **Ru•Mn**, but both complexes were characterised by high-resolution ES mass spectrometry (SI, Figs. S16 and S17). We note that seven coordination is known for in some Mn(II) complexes, and is supported by the calculations (see later).¹⁶ There are also a few examples of Zn(II) complexes with seven-fold coordination despite the smaller ionic radius of Zn(II): these generally have two small bidentate nitrate ligands.¹⁷

Trinuclear **Ru•Zn₂** and **Ru•Mn₂** were prepared similarly from **Ru•L₂** and excess (2.4 – 4.8 equivalents) of the appropriate M(II) chloride hydrate (M = Mn, Zn), and were obtained in good yields of 67 – 82 %. These are dianionic complexes with Na⁺ as the counter-cation. **Ru•Zn₂** could be characterised by ¹H NMR spectroscopy (SI, Fig. S18) and gives the correct number of signals in the aromatic and aliphatic regions which integrate to the required total: the spectrum is noticeably broader than that of **Ru•Zn**, likely due to slower tumbling in solution because of its size and the viscosity of D₂O (similar to the difference that we observed between **Ru•L** and **Ru•L₂**). As with **Ru•Zn** there is evidence that the presence of diastereoisomers arising from the presence of three chiral centres splits some signals into several components. For example, the singlet at δ = 7.69 ppm for the four pyridyl H³/H⁵ protons in **Ru•L₂** is split into two broad singlets between 7.50 and 7.70 ppm in the spectrum

of **Ru•Zn₂**. High resolution ES mass spectra confirmed the formulations of **Ru•Zn₂** and **Ru•Mn₂** (Figs. S19, S20).

(ii) Photophysical properties.

Mononuclear Ru(II) complexes.

All four mononuclear complexes **Ru•E**, **Ru•L**, **Ru•E₂** and **Ru•L₂** were characterised by UV/Vis and luminescence spectroscopy (Table 1, Fig. 1 and S21). The monosubstituted complexes **Ru•E** and **Ru•L** both show, in addition to the usual ligand-centred absorptions in the UV region, ¹MLCT absorptions spanning the 375 – 550 nm region with a maximum at around 440 nm in each case. These are assigned as Ru→bipy and Ru→phen ¹MLCT transitions by comparison with published spectra:¹⁸ we might expect the Ru→phen transition to be at lower energy given the alkyne substituent conjugated with the phen core which will reduce the energy of the LUMO, but any such effect is not clearly resolved in these spectra. However, for **Ru•E₂** and **Ru•L₂** the absorption spectra do clearly show this effect (Fig. S9): the second alkyne substituent on the phen ligand results in a Ru→phen ¹MLCT transition that is clearly apparent as a low-energy shoulder at *ca.* 480 nm with the more intense ¹MLCT Ru→bipy transition (as there are two bipy ligands) remaining at *ca.* 440 nm.

The luminescence spectra in fluid and frozen solution, at RT and 77 K respectively (Fig. 1), likewise reflect the general behaviour of [Ru(bipy)₃]²⁺-type cores¹⁸ where modification by the alkyne substituents slightly reduces the ³MLCT excited state energies.¹⁹ For **Ru•E** and **Ru•L** the broad, featureless ³MLCT emission band occurs at *ca.* 650 nm, slightly lower in energy than what has been observed for [Ru(bipy)₂(phen)]²⁺ bearing no alkyne substituents.^{8a} At 77 K (frozen EtOH/MeOH glass) the usual rigidochromism results in a blue-shift of the main emission maximum to 611 nm (hence, the ³MLCT energy is 16,400 cm⁻¹, measured from the 0-0 transition energy) and results in the appearance of clear fine-structure with two low-energy shoulders on the emission profile arising from vibronic effects. The presence of the additional alkyne substituent in **Ru•E₂** and **Ru•L₂** results in an additional red-shift of both the solution luminescence maximum to *ca.* 690 nm. The 77 K emission spectrum (frozen EtOH/MeOH glass) of **Ru•E₂** is likewise red-shifted to 645 nm

compared to **Ru•E** and **Ru•L**. **Ru•L₂** was not sufficiently soluble in EtOH/MeOH to permit a 77 K spectrum but it is clear from comparison of **Ru•E** and **Ru•L** that the presence or absence of the ester groups has no significant effect on the luminescence energy. This gives a ³MLCT excited-state energy of 15,500 cm⁻¹ for both **Ru•E₂** and **Ru•L₂**. Luminescence lifetimes in air-equilibrated solution at RT for all four complexes are in the region of 100 – 300 ns; these become longer (μs timescale) at 77 K (see Table 1).

Heteronuclear Ru•M and Ru•M₂ complexes (M = Gd, Nd, Yb).

UV/Vis absorption spectra in water (Table 2) revealed that coordination of the Gd(III) centre had little effect on the main spectral features which are of course associated with the Ru(II) *tris*-diimine core.¹⁸ Thus the absorption spectrum of **Ru•Gd** is similar to that of **Ru•L**. However, we can see that for **Ru•Gd₂** the lowest energy ¹MLCT absorption feature – a shoulder associated with the Ru→phen transition – is slightly red-shifted by about 10 nm compared to **Ru•L₂**. This can be ascribed to the electronic effect of a 3+ cation coordinated to each of the two pyridine groups pendant from the phen ligand, which will reduce the LUMO in energy and cause red-shifting of the associated Ru→phen absorption. Excitation into the ¹MLCT absorption profile afforded the characteristic broad, featureless (in fluid solution) ³MLCT luminescence band in each case, at 664 nm and 700 nm for **Ru•Gd** and **Ru•Gd₂**, respectively (Fig. 2). These are slightly red-shifted from the emission maxima for **Ru•L** and **Ru•L₂**, since coordination of the pyridyl groups pendant from the phen ligand to the 3+ ions reduces the LUMO energy slightly, which is also why a red-shift was observed in the absorption spectra. Photophysical data for these complexes, including luminescence lifetimes and quantum yields, are included in Table 2.

The UV/Vis absorption spectra for the Ru/Yb and Ru/Nd complexes in water are identical within experimental error to those of the analogous Ru/Gd complexes described earlier, as the electronic effects of the peripheral Gd(III), Nd(III) and Yb(III) ions on the absorption features of the Ru(II) *tris*-diimine core are essentially identical and thus require no further discussion. However, the effects of the different lanthanide ions on the luminescence are substantial and are most easily discussed in terms of comparison with the Ru/Gd complexes, as in these complexes Gd(III) is non-luminescent: the lowest excited state for the Gd(III) ion (⁶P_{7/2} ≈ 32,000 cm⁻¹) is far too high in energy to be directly populated by Ru→Gd PEnT.

Fig. 2 shows the emission spectra in the visible region of all six **Ru•Ln** and **Ru•Ln₂** complexes (Ln = Gd, Nd, Yb) in water, recorded on samples prepared to have the same optical density at the excitation wavelength of 430 nm, such that comparisons of emission intensities are a meaningful indication of quantum yield variations. It is immediately clear that (i) the emission maxima for all three **Ru•Ln₂** complexes is at longer wavelength (700 nm) than the emission maxima for all three **Ru•Ln** complexes (662 – 664 nm), for reasons discussed earlier, and (ii) the intensity of Ru(II)-based emission within each set of three complexes decreases in the order Gd > Yb > Nd. Thus, compared to **Ru•Gd**, the quenching arising from the presence of Yb(III) and then Nd(III) is 10 % and 45 %, respectively: and compared to **Ru•Gd₂**, the quenching arising from the presence of Yb(III) and then Nd(III) is 45 % and 90 %, respectively (Table 3).

This quenching of Ru(II)-based emission by Yb(III) and Nd(III) is a consequence of PEnT from the Ru(II)-based ³MLCT state to lower-lying f-f excited states of the relevant Ln(III) ions. The different degrees of quenching, arising from different extents of Ru→Ln PEnT, can be readily understood in terms of the spectroscopic overlap between donor and acceptor states.^{1a,20} Yb(III) has a single f-f excited state at *ca.* 10,200 cm⁻¹ (absorption at 980 nm) which overlaps only with the low-energy tail of the Ru(II)-based emission profile that has vanishingly small intensity at 980 nm. In contrast Nd(III) has a large number of closely-spaced f-f excited states between 10,000 cm⁻¹ and 15,000 cm⁻¹, in the region covered by the Ru(II)-based emission spectrum, so donor/acceptor overlap will be much better. Indeed, it is generally true that for excited states of donors in the visible region of the spectrum, Nd(III) is a far better energy acceptor than Yb(III) for this reason,^{1a,20} and we see this in both series of complexes **Ru•Ln** and **Ru•Ln₂**.

Time-resolved measurements on the Ru(II)-based luminescence allows the Ru→Ln PEnT rates to be quantified. For **Ru•Gd** the Ru(II)-based luminescence in air-equilibrated water at RT is 350 ns; in **Ru•Yb** and **Ru•Nd** the luminescence decay is dominated by shorter-lived components with τ = 73 ns and 22 ns respectively (Table 3), confirming the greater ability of the Nd(III) ion to act as a quencher of the Ru(II)-based excited state. A very small contribution to the luminescence decay from a long-lived decay component with τ \approx 300 ns (< 5 %) is ascribed to a trace of free **Ru•L**.

$$k_{\text{PEnT}} = 1/\tau_q - 1/\tau_u \quad (2)$$

Using equation 2 [where τ_u is the 'unquenched' lifetime of **Ru•Gd**, and τ_q is the partially quenched lifetime of the **Ru•Ln** complexes (Ln = Yb, Nd)] the Ru→Yb and Ru→Nd energy-transfer rates of $1.1 \times 10^7 \text{ s}^{-1}$ and $4.2 \times 10^7 \text{ s}^{-1}$, respectively, were estimated. These values are broadly comparable to what we observed in the Ir/Ln complexes based on the same ligand skeleton,^{6a} and these relatively high PEnT rates are a consequence of the fully conjugated pathway connecting the two metal complex components within each molecule.

The decay of the Ru(II)-based emission in **Ru•Gd₂** showed two components: a longer lifetime of $\tau_1 = 402 \text{ ns}$ (20% of total) and a dominant shorter component of $\tau_2 = 164 \text{ ns}$ (80 % of total emission intensity). We tentatively ascribed the presence of a second longer-lived component to the presence of different conformers of the complex arising from the presence of multiple diastereoisomers (see sections on the ¹H NMR spectra of the analogous Ru/Zn complexes, and conformational flexibility of dinuclear complexes studied computationally). In **Ru•Yb₂** and **Ru•Nd₂** the luminescence decay profiles are dominated by short-lived components with $\tau = 88 \text{ ns}$ and 18 ns for **Ru•Yb₂** and **Ru•Nd₂** respectively, with (again) a small amount of a long-lived component likely corresponding to traces of free **Ru•L₂**. Application of eq. 2 (taking $\tau_u = 164 \text{ ns}$, the dominant component of emission from **Ru•Gd₂**) yields energy-transfer rates of $5.3 \times 10^6 \text{ s}^{-1}$ (for Ru→Yb PEnT) and $4.9 \times 10^7 \text{ s}^{-1}$ (for Ru→Nd PEnT), again confirming that Nd(III) is a better energy-acceptor than Yb(III) in these complexes due to its higher density of excited states in the relevant spectral region.^{1a,20} Final proof that Ru→Ln PEnT has occurred in the Yb(III) and Nd(III) complexes is shown by the appearance of sensitised Ln(III)-based luminescence following excitation into the Ru(II)-based ¹MLCT absorption band of the complexes in D₂O (the deuterated solvent is used to minimise solvent-based quenching of the low energy lanthanide luminescence).²¹ Fig. 3 shows the spectra of **Ru•Yb₂** and **Ru•Nd₂**; those of **Ru•Yb** and **Ru•Nd** are similar. Both Yb(III)-containing complexes display a characteristic Yb(III)-based emission feature centred at 980 nm arising from the ²F_{5/2}→²F_{7/2} transition. Time-resolved measurements afforded Yb(III)-based luminescence lifetimes of 13 μs for **Ru•Yb** and 11 μs for **Ru•Yb₂** (Table 3). Lifetimes in this region are typical of Yb(III)-based luminescence in fluid solution where the effect of the solvent is minimised by encapsulation of the metal ion in a polydentate ligand,

and/or by deuteration of the solvent (as here).²² The two Nd(III)-containing complexes show luminescence bands at 1060 nm and 1380 nm, arising from the $^4F_{3/2} \rightarrow ^4I_J$ transitions ($J = 11/2$ and $13/2$), respectively. Time-resolved measurements on the 1060 nm signal afforded Nd(III)-based emission lifetimes of 0.8 μ s for **Ru•Nd** and 0.7 μ s for **Ru•Nd₂**. Again, these are typical values for Nd(III)-based emission in fluid solution when there are no OH oscillators in the solvent,²² with the much shorter luminescence from Nd(III) centres compared to Yb(III) arising from the lower energy associated with luminescence which is more readily quenched by molecular (or solvent) vibrations. Finally, excitation spectra – monitoring the Ln(III)-based emission intensity as a function of excitation wavelength – revealed areas of absorbance between 400 and 500 nm associated with the Ru(II)-based ¹MLCT transitions, confirming the occurrence of Ru→Ln PEnT in all cases (see SI, Fig. S22 for examples).

*Heteronuclear **Ru•M** and **Ru•M₂** complexes (M = Mn, Zn).*

UV/Vis absorption spectra for the set of four Ru/Mn and Ru/Zn complexes (Table 2) follow the same pattern that we saw with the Ru/Ln complexes, *i.e.* the absorption spectra are essentially the same as the complexes **Ru•Gd** and **Ru•Gd₂** with no significant contributions from the Mn(II) or Zn(II) ions, as would be expected given their high-spin d⁵ and d¹⁰ electronic configurations. To confirm that the low luminescence intensity from the Ru/Mn complexes is specifically associated with the presence of the Mn(II) ions, we compared the luminescence properties of the Ru/Mn complexes to the Ru/Zn analogues **Ru•Zn** and **Ru•Zn₂** (see Fig. 5). The substantial additional quenching caused by Mn(II) ions over Zn(II) ions – as shown by reduction in emission intensity by approximately 80 % – confirms the role of Mn(II) in the quenching.

This quenching could have two possible origins: (i) photoinduced electron-transfer (PET) from Mn(II) to the Ru(III) centre that is photo-generated in the $[Ru^{3+}\text{-phen}^{\bullet-}]$ ³MLCT state;²³ or (ii) photoinduced energy-transfer from the ³MLCT state to Mn(II), generating a d-d excited state of Mn(II) that cannot be populated by direct absorption from the ground state as it is spin-forbidden, but could be generated by energy-transfer from the Ru-based ³MLCT state acting as a sensitizer.²⁴ Assemblies based on Ru(II) chromophores connected to mononuclear or polynuclear Mn(II) units have been extensively studied because of their relevance to the PET properties of photosystem II in green plants. Indeed, Hammarström,

Åkermark and co-workers have demonstrated that Mn(II)→Ru(III) PET occurs in a series of Ru(III)/Mn(II) dyads in which the Ru(III) centre has been generated by photo-oxidation of a Ru(II) unit, provided the metal centres are close together.^{23a-c}

Time-resolved luminescence measurements on **Ru•Zn** and **Ru•Zn₂** (in air-equilibrated aqueous solution) revealed ³MLCT emission lifetimes that are similar to those of **Ru•Gd** and **Ru•Gd₂**. For **Ru•Zn** a single-exponential luminescence decay of 329 ns was observed; for **Ru•Zn₂** the decay profile fitted to two components with $\tau_1 = 301$ ns (55%) and $\tau_2 = 117$ ns (45%), very similar to what we also observed for **Ru•Gd₂**. We therefore propose – for the same reason as suggested earlier – that the two lifetimes arise from a mixture of diastereoisomers with different conformations. We note that in this case individual lifetimes may not have specific physical meaning, as it is a distribution of lifetimes (multiexponential decay) which has been fitted satisfactorily with a two-exponential model. In contrast the partial quenching in **Ru•Mn** and **Ru•Mn₂** leads to a shorter component dominating the ³MLCT emission decay profiles, with lifetimes of 91 ns for **Ru•Mn** and 21 ns for **Ru•Mn₂**. In both cases small contributions from a longer-lived component were also present, consistent with traces of free **Ru•L** and **Ru•L₂** being present due to loss of Mn(II) ions from the binding sites of **Ru•Mn** and **Ru•Mn₂** in the competitive solvent. However, the dominant short-lived components indicate quenching of the Ru(II) excited state by the Mn(II) ions: these emission lifetimes did not change significantly over a range of concentrations from 4 μ M to 90 μ M, *i.e.* the quenching processes in **Ru•Mn** and **Ru•Mn₂** are intramolecular.

The decreased luminescence lifetimes (tens of ns) are not the whole story however, since the limitation of our luminescence lifetime spectrometer (*ca.* 1 ns time resolution) means that any faster decay processes associated with *e.g.* rapid PET are not detectable on this instrument. To investigate whether any ultrafast processes were occurring on the timescale faster than 1 ns, the excited state dynamic behaviour of **Ru•Zn** and **Ru•Mn** was investigated using femtosecond transient absorption spectroscopy (TA). Here, **Ru•Zn** acts as a control since any inter-metal PET or PEnT processes that occur in **Ru•Mn** cannot occur in **Ru•Zn**. Excitation ($\lambda_{\text{exc}} = 400$ nm, 40 fs pulse, 3 mW) of a solution of either **Ru•Zn** or **Ru•Mn** in aerated water, followed by measurement of the absorption spectra at a series of time delays up to 5 ns, produced similarly shaped differential TA spectra for both complexes (Fig. 5a, 6a). There are negative signals (bleaches) of the MLCT transitions at 442/480 nm, and positive signals that have maxima at 367 nm and 456 nm present in both spectra, as

well as a broad absorption in the range 500-700 nm with a maximum at 620 nm. These transient spectral features approximately resemble those of the [phen]^{•-} radical anion in other reduced metal complexes such as [Re^ICl(CO)₃(phen^{•-})]⁻.²⁵ Thus the transient absorption spectra are in agreement with the initial population of an MLCT state in both cases.

Analysis of the dynamics of the transient signals for each of the heteronuclear complexes reveals different decay kinetics for **Ru•Zn** and **Ru•Mn**. The dynamic behaviour of **Ru•Zn** (Fig. 5b) is described by two lifetime components; a long-lived component (blue trace in the figure) that does not completely decay over the pump-probe delay period, and a much shorter-lived component (red trace) with a lifetime of 6 ps. Decay-associated spectra for the different lifetime components are in SI (Fig. S23). The shorter-lived component can be ascribed to fast vibrational cooling within the complex, whereas the longer-lived component can be ascribed to the Ru-based ³MLCT state, for which an emission lifetime was measured as 329 ns in aerated water (see earlier). An accurate lifetime for the ³MLCT state could not be determined by femtosecond TA as it is much longer than the maximum possible time delay of the experiment.

The dynamic behaviour of the transient absorption spectra for **Ru•Mn** is more complicated than for **Ru•Zn** (Fig. 6b), and requires three lifetime components to fit the decay profile satisfactorily. A short-lived component with a lifetime of 2 ps (green trace) is ascribed to fast vibrational cooling within the complex. A further decay process with a lifetime of 584 ps (red trace) is synchronous with the grow-in for a second state which then decays more slowly, with an estimated lifetime of 4.7 ns (blue trace). As the processes on these timescales are not present in **Ru•Zn**, we suggest that they are a consequence of fast processes occurring between metal centres in the excited state of **Ru•Mn**, with one component decaying at the same rate as the other grows, in a PET or PEnT process. Again, decay-associated spectra for the different lifetime components are in SI (Fig. S23), and the evolution-associated spectra (experimental TA at different time delays) for both **Ru•Zn** and **Ru•Mn** are in Fig. S24.

If the 584 ps decay process were PEnT from the Ru(II)-based ³MLCT state to the Mn(II) centre, we would see decay of the intense (phen^{•-}) transient signal with $\tau = 584$ ps as the ³MLCT state converted to a [Mn(II)]^{*} state. However, this is clearly not the case. There is a small change in shape of the (phen^{•-}) transient signal on this timescale, but it only

decays on the longer timescale of $\tau = 4.7$ ns. This is consistent with the 584 ps process being Mn(II)→Ru(III) PET in which the bridging (phen^{•-}) is preserved, *i.e.* the process can be written as Mn^{II}–(phen^{•-})–Ru^{III} → Mn^{III}–(phen^{•-})–Ru^{II}, generating a new and lower-energy Mn^{III}/(phen^{•-}) MLCT state which then decays with $\tau = 4.7$ ns (and is not visible by luminescence spectroscopy).

The occurrence of Mn(II)→Ru(III) PET into the Ru-based ³MLCT state is in agreement with previous reports of the behaviour of [Ru(bipy)₃]²⁺/Mn(II) dyads following photochemical oxidation of Ru(II) to Ru(III),^{23a-c} which simply requires that the Mn(II)/Mn(III) redox potential is less positive than the Ru(II)/Ru(III) redox potential. Attempts to determine the Mn(II)/Mn(III) redox potential of **Ru•Mn** by cyclic voltammetry in water were unsuccessful possibly because the large excess of electrolyte used (NaCl) resulted in the Mn(II) ion being stripped out of the complex. Similar issues have occasionally prevented detection of Mn(II)/Mn(III) couples in other Ru/Mn complexes recorded in competitive media.^{23c} **Ru•Mn** is not sufficiently soluble in polar organic solvents such as MeCN or DMF to allow electrochemical measurements to be made. However we note that (i) the harder N/O-donor anionic ligand donor set around the Mn(II) ions in **Ru•Mn** and **Ru•Mn₂**, compared to the all-nitrogen donor sets used in the Hammarström/Åkermark complexes, will reduce the Mn(II)/Mn(III) redox potential which will facilitate the PET process; and (ii) the computational studies (next section) confirm that the Mn(II) centre oxidises before the Ru(II) centre, as required.

Assuming that the lifetime of the PET process in **Ru•Mn** is 584 ps, the rate of ET can be estimated as $k_{\text{et}} = 1.7 \times 10^9 \text{ s}^{-1}$. This PET rate is much faster than was previously observed by Hammarström, Åkermark and co-workers who reported PET rates in the range $k_{\text{et}} = 2 \times 10^5 - 2 \times 10^6 \text{ s}^{-1}$;^{23a-c} indeed it is faster than the radiative decay rate of the Ru(II) chromophore. Thus, the Mn(II)→Ru(III) process occurs rapidly in the Mn^{II}–(phen^{•-})–Ru^{III} excited state, and does not require photo-oxidation of this state to generate a long-lived Mn^{II}–(phen)–Ru^{III} species before the Mn(II)→Ru(III) ET can occur. This high ET rate can be ascribed to the presence of a favourable pathway through the conjugated bridging ligand in **Ru•Mn**, which provides a “conductive” bridge for the ET process to occur, in contrast to the saturated bridging ligands described previously.^{23a-c}

Given that this PET process detected by TA spectroscopy is fast (sub-nanosecond timescale) the final question arises as to why it does not always occur, as shown by the observation of significant residual luminescence (see Fig. 4; $\tau = 91$ ns for **Ru•Mn** and 21 ns for **Ru•Mn₂**). This can be ascribed to the presence of a mixture of conformers, as implied by some of the NMR studies (Ru/Zn complexes) and other luminescence measurements (Ru/Gd complexes). Rotation of the pyridyl group and its pendant aminocarboxylate units about the C-C single bond at the pyridyl C⁴ position could lead the pyridine ring to adopt a conformation perpendicular to the phen unit, which would electronically decouple the Mn(II) ion from the {Ru(bipy)₂(phen)}²⁺ core. In this arrangement, through-bond PET would be much slower. If we assume this to be the case, we arrive at Mn(II)→[Ru(III)]* PET rate constants k_{PET} (using eq. 2) of *ca.* $8 \times 10^6 \text{ s}^{-1}$ in **Ru•Mn** and $4 \times 10^7 \text{ s}^{-1}$ in **Ru•Mn₂** for those decoupled conformers in which PET is slow, which is still fast compared to the timescale of Mn(II)→Ru(III) ET across saturated spacers in several dyads.^{23a-c} To investigate this further, computational studies were performed on **Ru•Mn** using density functional theory.

*Computational studies on the **Ru•Mn** dyad.*

All calculations were performed using the procedures outlined in the experimental details section. The structure of the lowest sextet state of **Ru•Mn** is given in Fig. 7(a). For a Mn(II) ion in this N/O-donor weak-field coordination environment we expect a high-spin configuration, which is what the spin density shows [Fig. 7(b)]. The Mn(II) ion is seven coordinate¹⁶ with an approximately pentagonal bipyramidal coordination geometry.^{16d} The three N-donor atoms are 2.5 Å from Mn(II), whereas the four Mn–O distances are shorter at *ca.* 2.2 Å, reflecting the partial negative charges on the carboxylate O atoms. The pyridine N-donor is approximately co-planar with two of the carboxylate O-donors: one of the amine donors is slightly below this plane with the other amine donor a similar distance above it. However, to a first approximation, the Mn(II) ion is pentagonal bipyramidal.

Given the possibility for conformational flexibility which might affect the electronic coupling between the two metal complex units, as discussed above, we looked at the barrier to rotation of the Mn(II) unit with respect to the Ru(II) core, around the C-C single bond between the alkyne linker and the pendant pyridyl ring. Calculations on this rotation show that an arrangement with the pendant pyridine unit perpendicular to the phenanthroline unit is not a local minimum. However, the energy of this ‘perpendicular’

arrangement is only 4.6 kJ mol^{-1} (or 1.8 kT) above the energy of the co-planar orientation [Fig. 7(a)]. This small energy difference means that rotation around the C–C bond is quite facile such that a large part of the torsional space will be sampled in solution at RT. This includes torsional conformations in which the pyridyl [coordinated to Mn(II)] and phen [coordinated to Ru(II)] units are orthogonal to each other and substantially electronically decoupled, in agreement with our explanation of the two observed PET rates for **Ru•Mn**. The overlay in Fig. 8(a) shows that rotation around this bond has little structural effect on the Ru(II) moiety.

TD-DFT calculations on the structure with a planar orientation of the bridging ligand [Fig. 7(a)] show that there are only a small number of strong electronic transitions (Fig. 9). Inspection of the major components of these transitions (see computational SI document) shows that all strong transitions at wavelengths longer than 450 nm are essentially Ru→phen MLCT states, in agreement with a wealth of precedent,¹⁸ generating a local Ru(III)/phen^{•−} moiety in a triplet excited state. Depending on the interaction between this complex unit in its ³MLCT excited state, and the sextet state of the Mn(II) ion, overall either a quartet or an octet state can arise following photo-excitation of the Ru(II) centre. Our calculations show that the quartet state is the lower of the two possibilities, indicating weak antiferromagnetic coupling between the Ru(III)/phen^{•−} (triplet) and Mn(II) (sextet) moieties. If this quartet state is optimized, then the resulting electron distribution will reflect the relaxation by PET from Mn(II) to the short-lived Ru(III) centre, and the structure depicted in Fig. 7(c) is obtained. The associated spin density shows that the molecule in this state has no spin density on Ru, *i.e.* the Ru centre is now Ru(II), and there is β -spin density on the phen ligand, indicating a phen^{•−} species. As a result, the formal charge on Mn should be 3+: this is also evident from our inspection of the coordination geometry around this ion which reveals substantial shortening of all of the Mn-ligand bond distances [*cf.* the overlay of the ground-state sextet geometry of **Ru•Mn** and this quartet excited state, Fig. 8(b)]. The equatorial metal-ligand bond distances reduce by 0.1 \AA (all amine and oxygen donors) or by 0.2 \AA (pyridine N donor). The axial bond distances reduce by 0.4 \AA . Thus a $\text{Mn}^{\text{III}}-(\text{phen}^{\bullet-})-\text{Ru}^{\text{II}}$ state is shown to be the lowest-energy state following photo-excitation, confirming the occurrence of the PET process that was implied by the TA measurements: this is the species that has a lifetime of 4.7 ns according to transient absorption data.

Rotation of the pyridyl unit around the C–C bond separating it from the alkyne linker to give the ‘perpendicular’ orientation mentioned earlier increases the energy of the quartet excited state by 25.1 kJ mol⁻¹ (or 10.1 kT) compared to the co-planar arrangement – a considerably larger difference that was found for the ground state. This suggests that in the quartet Mn^{II}–(phen^{•-})–Ru^{III} excited state there is less torsional motion of the pyridyl unit with respect to the phenanthroline unit, such that the perpendicular arrangement in the quartet state can only be accessed from the same arrangement in the sextet state.

Further confirmation of the occurrence of the intramolecular PET process is provided by examination of the localisation of redox processes in ground-state **Ru•Mn**. Fig. 8(c) and 8(d) show the overlay of **Ru•Mn** with **Ru•Mn⁺** and **Ru•Mn⁻**, respectively. Both oxidised and reduced species were geometry-optimized in the quintet state. The overlay between **Ru•Mn** and **Ru•Mn⁺** shows a similar structural change to that seen in the overlay between the sextet and quartet states of **Ru•Mn**, as shown in Fig. 8(b). This indicates that one-electron oxidation does indeed happen at the Mn centre, yielding a formal charge of 3+, and that this is therefore the site of the first oxidation. This localisation for the first oxidation process is also evident if one considers the difference in the total electron density between **Ru•Mn⁺** (at the geometry of **Ru•Mn**) and **Ru•Mn** as depicted in 7(e): there is a decrease in electron density on the Mn moiety consistent with formation of Mn(III), but the electron density of the Ru(II) centre does not change upon one-electron oxidation of the complex.

In contrast, upon reduction of **Ru•Mn** to **Ru•Mn⁻** there is almost no structural change, as is clear from the overlay in Fig. 8(d). The difference electron density shown in Fig. 7(f) (between **Ru•Mn⁻** and **Ru•Mn** at the **Ru•Mn⁻** geometry) confirms that the one-electron reduction is associated with the phen ligand. These observations from computational studies support our experimental findings.

(iii) Applications for imaging: relaxivity properties and luminescence imaging studies

Ru/Gd complexes.

Relaxivity measurements for **Ru•Gd** and **Ru•Gd₂** were performed at 400 MHz and 298 K in D₂O by the inversion-recovery technique, alongside the commercial contrast agent Magnevist® for comparison purposes. Solutions of each complex were prepared at five different concentrations (0 – 2.0 mM) and the longitudinal relaxation time (*T*₁) for the

residual H₂O peak in each sample was measured using a standard inversion-recovery pulse sequence. The concentration-normalised longitudinal relaxivity value (r_1) for each complex was then determined from a linear plot of longitudinal relaxation time against contrast agent concentration (SI, Fig. S25) in accordance with eq. 1:

$$1/T_1^{\text{obs}} = 1/T_1^0 + r_1[M] \quad (1)$$

where r_1 is the relaxivity value, $[M]$ is the complex concentration, T_1^{obs} is the observed T_1 value in the presence of complex, and T_1^0 is the value of T_1 in the absence of any complex. Under the conditions used the reference compound Magnevist® has $r_1 = 4.6 \text{ mM}^{-1} \text{ s}^{-1}$, and our new compounds **Ru•Gd** and **Ru•Gd₂** have $r_1 = 6.2$ and $13.6 \text{ mM}^{-1} \text{ s}^{-1}$, respectively. The increase in relaxivity between Magnevist® and both Ru/Gd complexes can be ascribed to a combination of greater complex bulk (and hence slower tumbling in solution) for **Ru•Gd** and **Ru•Gd₂**, and possibly also the fact that the Gd(III) ion binding site in both Ru/Gd complexes is heptadentate, which leaves room for potentially two water molecules ($q = 2$), whereas Magnevist® has $q = 1$. In fact the q value for a Eu(III) complex with the same aminocarboxylate donor set was previously determined as 1.6 ± 0.5 ,^{6a} implying a mixture of mono- and di-aqua coordination in solution. These r_1 values compare favourably with those for other oligonuclear complexes.^{4a}

Given the promising relaxivity properties of **Ru•Gd** and **Ru•Gd₂** we were also interested to see if the Ru(II)-based luminescence could be used as the basis of cellular imaging. Live HeLa cells were initially incubated with either of these complexes at concentrations of 25 μM , 50 μM and 75 μM for six or sixteen hours. Cells stained with either of the probes for the longer incubation period (16 h) at all concentrations were visually unhealthy when viewed under the microscope, and cells stained with the lowest concentration of the probes (25 μM) demonstrated only weak Ru(II)-based emission even at the longer incubation times. These results suggested, therefore, that shorter incubation times and higher concentrations would provide the optimum imaging conditions for both complexes. Accordingly, further cellular staining was conducted with live HeLa cells incubated with probe concentrations of 50 μM , 75 μM and 100 μM for four hours, or with an increased probe concentration (75 μM , 100 μM and 150 μM) over a shorter incubation period (two hours). In this instance all of the cells stained for each incubation time and at

each concentration for both probes were visually healthy when viewed under the microscope, apart from the cells incubated with a probe concentration of 150 μM , which were beginning to detach from the sterile coverslip.

Ru(II)-based emission was observed from all of the healthy cells when imaged with a confocal microscope ($\lambda_{\text{exc}} = 405 \text{ nm}$, $\lambda_{\text{em}} = 570\text{-}620 \text{ nm}$): however, the emission from the cells incubated for only 2 h (with either complex) was weak, suggesting lower cellular uptake. The optimum imaging conditions for each complex were found to be an incubation time of 4 h using a concentration of 50 μM , which allowed for reasonable cellular uptake without high levels of cytotoxicity being observed. Example emission images of HeLa cells incubated with **Ru•Gd** and **Ru•Gd₂** (Fig. 10) show punctate cytoplasmic staining, suggesting that both of the probes localise in a specific organelle within the HeLa cells, such as the lysosomes or the mitochondria. Co-localisation studies with the commercial lysosomal and mitochondrial stains LysoTracker® Red and MitoTracker® Red were not successful as some absorbance of these stains at the excitation wavelength used (405 nm) produced red luminescence which interfered with that of the Ru(II) complexes.

The cytotoxicity of **Ru•Gd** and **Ru•Gd₂** towards HeLa cells under the optimum imaging conditions (50 μM , 4 h) and also at an increased probe concentration (200 μM , 4 h) was assessed by clonogenic assay (SI, Fig. S26). Both of the complexes exhibited low toxicity under the conditions used to image the cells, with survival fractions of > 0.85 being observed in both cases. Increasing the probe concentration four-fold to 200 μM had the expected effect of lowering the cell survival fraction in comparison to the lower concentration, but good survival levels were still observed for both probes (> 0.8). The trinuclear probe **Ru•Gd₂** causes lower cell survival fractions at both probe concentrations when compared to dinuclear **Ru•Gd**. Overall, the ability of these complexes to act as stains in luminescence imaging – in addition to providing high relaxivity for water protons – is clear.

Ru/Mn complexes

To see how the Mn(II) centres fared for relaxivity purposes compared to Gd(III), relaxivity experiments on **Ru•Mn** and **Ru•Mn₂** were carried out in D₂O at 400 MHz and 298 K, alongside the commercial Gd(III)-based contrast agent Magnevist® for comparison purposes (SI, Fig. S27). Exactly the same methodology was used as for the Ru/Gd

complexes, affording relaxivity values of $r_1 = 3.7 \text{ mM}^{-1} \text{ s}^{-1}$ and $4.8 \text{ mM}^{-1} \text{ s}^{-1}$ for **Ru•Mn** and **Ru•Mn₂** respectively, which compare favourably to a range of mononuclear Mn(II) complexes in a similar N/O-donor coordination environment based predominantly on amine and carboxylate ligands.^{14c} Under the same experimental conditions, Magnevist® has a relaxivity value of $r_1 = 4.6 \text{ mM}^{-1} \text{ s}^{-1}$. We recall that **Ru•Gd** and **Ru•Gd₂** have larger relaxivity values ($r_1 = 6.2 \text{ mM}^{-1} \text{ s}^{-1}$ and $13.6 \text{ mM}^{-1} \text{ s}^{-1}$, respectively). The smaller relaxivity values for the Ru/Mn complexes compared to the Ru/Gd analogues are of course principally attributable to the smaller magnetic moment of Mn(II) compared to Gd(III), but the smaller number of water molecules coordinated to the metal centre in solution will be significant too. In Magnevist® the Gd(III) ion is 9-coordinate from an octadentate DTPA ligand and one water molecule, whereas the smaller Mn(II) ion in the same ligand is coordinatively saturated by the ligand ($q = 0$).^{14d} We observed a hydration number of 1.6 ± 0.5 for Eu(III) ions in the heptadentate binding site used in these complexes,^{6a} and by analogy with the DTPA complexes this value will be smaller when Mn(II) is coordinated at the same binding site due to its smaller size and preference for lower coordination numbers. Although **Ru•Mn₂** does show relaxivity similar to that of Magnevist®, its use as a dual magnetic resonance / luminescence imaging agent is inhibited by the fact that the Ru(II)-based ³MLCT luminescence is partly quenched by the Mn(II) ions; the same is true for **Ru•Mn**.

Conclusion

The ligand skeleton containing a phenanthroline unit (for coordination to a photosensitising complex core) with one or two pendant pyridyl/aminodicarboxylate units connected *via* alkyne linkages has been used to prepare a variety of d/d and d/f heterodinuclear and heterotrinnuclear complexes. The central photosensitising unit is {Ru(bipy)₂(phen)}²⁺ in all cases. The secondary metal ions at the pendant sites are either from the f-block [Gd(III) for its relaxivity; Nd(III) or Yb(III) for their near-infrared luminescence] or the d-block [Mn(II) for its relaxivity and ability to effect PET to the excited state of the Ru(II) unit; and Zn(II) as a control for comparison with the Mn(II) complexes].

A range of interesting behaviours has emerged. The complexes **Ru•Gd** and **Ru•Gd₂** show relaxivity of water protons that is high for the number of Gd(III) ions that they contain because of their size and, therefore, slow rotation in solution; in addition they retain the characteristic phosphorescence of the {Ru(bipy)₂(phen)}²⁺ core which can be used for

luminescence imaging of cells such that they have potential as dual (luminescence and MRI relaxivity) imaging agents. The analogous Ru/Yb and Ru/Nd complexes display Ru→Yb and Ru→Nd (respectively) photoinduced energy-transfer, leading to partial quenching of the Ru(II)-based emission and sensitised near-infrared luminescence from the lanthanide unit. The energy-transfer to Nd(III) is much faster than to Yb(III) because of the higher density of f-f excited states in the correct spectral region on Nd(III), which can act as energy acceptors.

In the Ru/Mn complexes **Ru•Mn** and **Ru•Mn₂** the presence of the Mn(II) ions likewise provide a basis for relaxivity of water protons, with relaxivity values competitive with other Mn(II)-based complexes. In this case however the phosphorescence of the {Ru(bipy)₂(phen)}²⁺ core is substantially quenched by the Mn(II) ions – similar quenching does not occur when Mn(II) is replaced by Zn(II). Ultrafast transient absorption experiments on **Ru•Mn** (and **Ru•Zn** as a control) reveal the presence of fast (< 1 ns) PET from the Mn(II) ion to the Ru(II)-based ³MLCT state, *i.e.* Mn^{II}–(phen^{•-})–Ru^{III} → Mn^{III}–(phen^{•-})–Ru^{II}. The resulting Mn^{III}–(phen^{•-}) state decays with $\tau \approx 5$ ns and is non-luminescent. This fast quenching mechanism does not always occur, as shown by the presence of residual Ru(II)-based luminescence in **Ru•Mn** and **Ru•Mn₂** (tens of ns lifetime), which we ascribe to the presence of a conformer in which the central and peripheral metal complex centres are decoupled by rotation of the pyridyl units such that they are perpendicular to the phen unit.

Experimental

General details.

All reagents, unless otherwise stated, were purchased from commercial sources (Sigma-Aldrich, Alfa Aesar, Fluorochem) and used as received. All solvents were of HPLC grade quality and obtained from Fisher, excluding deuterated solvents (Sigma-Aldrich, Acros Organics, VWR). Dry solvents were obtained from the Grubbs dry solvent system at the University of Sheffield. The following materials were prepared using literature procedures: 4-bromo-2,6-bis[*N,N*-bis(*tert*-butoxycarbonylmethyl)aminomethyl]pyridine (compound **B**),¹² 3-bromo-1,10-phenanthroline,⁹ 3,8-dibromo-1,10-phenanthroline,⁹ [Ru(bipy)₂Cl₂]•2H₂O.²⁶

Instrumentation.

One-dimensional ¹H and ¹³C NMR spectra and two-dimensional COSY spectra were recorded using either a Bruker Avance III HD 400 spectrometer or a Bruker Avance III HD 500 spectrometer. Electrospray ionisation (ES) mass spectra were recorded on an Agilent Technologies 6530 Accurate-Mass Q-TOF LC/MS instrument (University of Sheffield). High-resolution spectra were recorded on a Bruker MaXis plus instrument (University of Warwick). UV/Vis spectra were measured on a Varian Cary 50 Bio UV-Visible Spectrophotometer.

Photoluminescence spectra were recorded on a Horiba Jobin Yvon Fluoromax-4-Spectrofluorimeter and were corrected using correction files included within the FluorEssence™ software. Near-IR emission and excitation spectra of the Yb(III) and Nd(III) complexes were recorded on an Edinburgh Instrument FP920 Phosphorescence Lifetime Spectrometer equipped with a 450 watt steady state xenon lamp; a 5 watt microsecond pulsed xenon flashlamp (with single 300 mm focal length excitation and emission monochromators in Czerny Turner configuration); a red sensitive photomultiplier in a Peltier (air cooled) housing (Hamamatsu R928P); and a liquid nitrogen cooled NIR photomultiplier (Hamamatsu), and were corrected using correction files included within the software. Near-IR emission spectra were recorded using a 645 nm longpass filter. Low-temperature emission spectra in the visible region were measured in frozen (77 K) glasses of ethanol/methanol (4:1, v:v). Decay curves generated by single photon counting (SPC) were

fitted using Origin[®] software and the quality of fit judged by minimization of reduced chi-squared and sum-of-residuals squared values.

NMR relaxivity measurements.

Relaxivity measurements for **Ru•Gd**, **Ru•Gd₂**, **Ru•Mn**, **Ru•Mn₂** and the commercial contrast agent gadopentetic acid ('Magnevist[®]') were performed on a Bruker Avance III 400 spectrometer at 298 K. Each compound under investigation was dissolved in D₂O at five different concentrations (0 – 2.0 mM) and the spin-lattice relaxation time (T_1) for the residual H₂O peak in each sample measured using a standard inversion-recovery pulse sequence with 12 recovery times varying between 0.001-60 seconds for gadopentetic acid and 15 recovery times varying between 0.001-15 seconds for the four new complexes. Relaxivity values were determined from a linear plot of spin-lattice relaxation time (T_1) against contrast agent concentration (0 – 2.0 mM) in accordance with eq. 1.

Cell imaging studies.

HeLa cells were cultured in Dulbecco's modified eagle medium (DMEM, high glucose with L-glutamine) purchased from Lonza (500 mL) and supplemented with 10 % (v/v) foetal bovine serum (FBS). Cultures were grown as monolayers in T-75 flasks at 37 °C in a 5 % CO₂ / 95 % air (v/v) environment. Once at 75-80 % confluency, cells were subcultured using trypsin- EDTA (2 mL). Subcultures for live cell staining were seeded on to sterile coverslips (15 mm x 15 mm) in 6-well plates (100,000/well) and those for clonogenic assays were seeded directly in to 6-well plates (200-400/well). All subcultures were incubated in DMEM at 37 °C in a 5 % CO₂ / 95 % air (v/v) environment overnight to allow for adhesion to the well-plate or coverslip.

For cell staining, **Ru•Gd** and **Ru•Gd₂** were dissolved in sterile, double-distilled water to form stock solutions with a concentration of 1 mM. Further dilution to generate working solutions of 50-200 µM was achieved using DMEM supplemented with 10 % (v/v) FBS. After removal of the growth media, cells were washed with sterilised phosphate-buffered saline (PBS, 3 x 2 mL/well) before being treated with a solution of the appropriate Ru/Gd complex at concentrations of 50 – 200 µM (2 mL/well). Cells were incubated for 2 h or 4 h at 37 °C in DMEM in a 5 % CO₂ / 95 % air (v/v) environment. After the desired incubation time the growth medium was removed and the cells were washed with PBS (3 x 2 mL/well) to remove excess metal complex. The cells were then treated with paraformaldehyde solution

(4 % in PBS, 1 mL/well) for 20 minutes, before being washed again with PBS (3 x 2 mL/well). The coverslips were mounted on to microscope slides (Immu-Mount™, Thermo Scientific) and left to dry for a minimum of 30 minutes before imaging. Confocal images of fixed HeLa cells were recorded using an inverted Nikon A1 confocal microscope with a 60x lens (CFI Plan Apochromat VC 60x oil, NA 1.4). A diode laser (405 nm) was used for excitation of the Ru/Gd complexes and a 570-620 nm emission filter was used.

Toxicity assay

After removal of the growth media, live HeLa cells were treated with a solution of **Ru•Gd** or **Ru•Gd₂** complex in media at both 50 μ M and 200 μ M (1 mL/well). Cells in four control wells were left untreated and immersed in DMEM (2 mL/well). Cells were incubated for 4 h at 37 °C in a 5 % CO₂ / 95 % air (v/v) environment. Following incubation, the treatment solution was removed, and the cells immersed in fresh DMEM (2 mL/well) and incubated for seven to ten days at 37 °C in a 5 % CO₂ / 95 % air (v/v) environment until visible cell colonies had formed. The growth medium was removed, and the cells were fixed and stained with methylene blue in methanol (4 g/L) for a minimum of 30 minutes. The staining solution was removed, and the number of colonies counted, with each colony representing a surviving cell. The ‘survival fraction’ for cells treated with the Ru/Gd complexes is the number of colonies formed after treatment with Ru/Gd complexes compared to controls in the absence of complex. Experiments were conducted in duplicate for seeding densities of 200 and 400 cells/well and repeated on three separate occasions. Survival fractions quoted are averages of the three repeats.

Transient absorption spectroscopy measurements

A Ti:Sapphire regenerative amplifier (Spitfire ACE PA-40, Spectra-Physics) provided 800 nm pulses (40 fs fwhm, 10 kHz, 1.2mJ); 400 nm for sample excitation was provided by doubling a portion of the 800 nm output, in a β -barium borate crystal within a commercially available doubler/tripler (TimePlate, Photop Technologies). White light, supercontinuum, probe pulses were generated *in situ* by using a portion of the Ti:sapphire amplifier output, focused onto a CaF₂ crystal, allowing for the generation of light spanning 340 – 790 nm. Detection was achieved using a commercial transient absorption spectrometer (Helios, Ultrafast Systems) and was performed by a CMOS sensor for the UV/Vis spectral range. The

relative polarisation of the pump and probe pulses was set to the magic angle of 54.7° for anisotropy-free measurements. Samples were held in 1 mm path length quartz cells. The optical density at the excitation wavelength was kept at approximately 0.5. The optical density across the probe range was kept below 0.8.

Excited state dynamics were elucidated by global lifetime analysis, performed in Glotaran.²⁷ Difference spectra were baseline corrected through subtraction of an average of the pre-excitation spectra. Sequential kinetic models were then applied to each dataset to model the excited state dynamics. A polynomial curve was fit to the data to account for the group velocity dispersion of the probe light in the kinetic model. The number of lifetime components was systematically varied in order to minimise the residual intensity between the experimental and model data, where the minimum χ^2 value had been obtained.

Synthesis

4-(Trimethylsilyl)ethynyl-2,6-bis[*N,N*-bis(*tert*-butoxycarbonylmethyl)-aminomethyl]pyridine (compound **C^{Si}).** A mixture of 4-bromo-2,6-bis[*N,N*-bis(*tert*-butoxycarbonylmethyl)-aminomethyl]pyridine (compound **B**; 6.89 g, 10.2 mmol), Pd(PPh₃)₂Cl₂ (0.50 g, 0.712 mmol), CuI (0.30 g, 1.58 mmol) and PPh₃ (0.10 g, 0.381 mmol) were added to anhydrous ⁱPr₂NH (30 cm³) and the mixture deoxygenated with argon gas for 30 minutes. Trimethylsilyl-acetylene (15 cm³, 108 mmol) was added with vigorous stirring and the resulting mixture heated at 83 °C for 24 hours. Once cooled, the reaction was filtered through celite® and washed with CH₂Cl₂ until the washings ran clear. The solvent was then removed under reduced pressure to afford a black residue, which was flash-filtered through silica gel (200-300 mesh) with CH₂Cl₂ as eluent. The crude product was then purified further using column chromatography on silica gel (200-300 mesh) with petroleum ether/ ethyl acetate (9:1 to 8:2, v:v) as the eluent to afford 4-(trimethylsilyl)ethynyl-2,6-bis[*N,N*-bis(*tert*-butoxy-carbonylmethyl)aminomethyl]pyridine (**C^{Si}**; 4.25 g, 60 %) as a dark yellow oil. ¹H NMR (400 MHz, CDCl₃): δ = 0.18 (s, 9H, SiMe₃); 1.42 (s, 36H, ^tBu); 3.43 (s, 8H, NCH₂-ester); 3.96 (s, 4H, NCH₂-pyridyl); 7.48 (s, 2H, pyridyl H³/H⁵). ESMS: m/z = 690.4 [$M + H$]⁺, 712.4 [$M + Na$]⁺.

4-Ethynyl-2,6-bis[*N,N*-bis(*tert*-butoxycarbonylmethyl)-aminomethyl]pyridine (compound **C).** Protected compound **C^{Si}** (0.75 g, 1.09 mmol) and tetra-*n*-butylammonium fluoride (0.43 g, 1.63 mmol) were dissolved in THF (45 mL) and stirred at RT for 16 hours.

The solvent was then removed under reduced pressure and the resulting residue dissolved in CH₂Cl₂ (30 cm³), washed with water (2 x 30 cm³) and dried (MgSO₄). The solvent was removed under reduced pressure to afford compound **C** (0.62 g, 92 %) as a dark yellow oil. Due to the reactivity of the alkyne substituent this compound was used immediately after preparation without further characterisation.

[Ru(bipy)₂(Br-phen)](PF₆)₂ (compound A). A mixture of 3-bromo-1,10-phenanthroline (0.95 g, 3.68 mmol) and *cis*-[Ru(bipy)₂Cl₂]•2H₂O (1.90 g, 3.65 mmol) in CH₃OH (30 cm³) was heated to reflux for 16 hours. Once cooled, the solution was concentrated under reduced pressure and an excess of saturated KPF_{6(aq)} solution (20 cm³) was added. The solution was left at 4 °C for 16 hours and the resulting precipitate dissolved in CH₂Cl₂ (30 cm³) and washed with water (3 x 25 cm³). The combined aqueous layers were then re-extracted with further portions of CH₂Cl₂ (2 x 25 cm³) and the resulting organic extracts combined and dried (MgSO₄). The solvent was removed under reduced pressure to afford compound **A** (3.51 g) as a red solid in quantitative yield. ¹H NMR (400 MHz, d₆-acetone): δ = 7.36-7.42 (m, 2H, bipy); 7.60-7.66 (m, 2H, bipy); 7.85 (dd, 1H, *J* = 1.5 and 5.6 Hz, bipy); 7.94 (dd, 1H, *J* = 5.2 and 8.2 Hz, phen); 8.04 (dd, 1H, *J* = 1.5 and 5.6 Hz, bipy); 8.10 (dd, 1H, *J* = 1.5 and Hz, bipy); 8.12-8.18 (m, 2H, bipy); 8.19 (dd, 1H, *J* = 1.5 and 5.6 Hz, bipy); 8.25 (tt, 2H, *J* = 1.5 and 7.9 Hz, bipy); 8.35 (d, 1H, *J* = 8.9 Hz, phen); 8.44 (dd, 1H, *J* = 1.2 and 5.2 Hz, phen); 8.45 (d, 1H, *J* = 8.9 Hz, phen); 8.47 (d, 1H, *J* = 1.9 Hz, phen); 8.78 – 8.87 (m, 5H, 4 x bipy, 1 x phen); 9.06 (d, 1H, *J* = 1.9 Hz, phen). ESMS: *m/z* = 337 [*M* – 2PF₆]²⁺. High resolution ESMS: *m/z* = 337.0101 (calculated for [C₃₂H₂₃N₆BrRu]²⁺, 337.0099).

[Ru(bipy)₂(Br₂-phen)](PF₆)₂ (compound D). This was prepared from 3,8-dibromo-1,10-phenanthroline (0.33 g, 0.98 mmol) and *cis*-[Ru(bipy)₂Cl₂]•2H₂O (0.51 g, 0.98 mmol) exactly as described above for complex **A**, to afford compound **D** (1.02 g) as a red solid in quantitative yield. ¹H NMR (400 MHz, d₆-acetone): δ = 7.40 (ddd, 2H, *J* = 1.2, 5.6 and 7.9 Hz, bipy); 7.63 (ddd, 2H, *J* = 1.2, 5.6 and 7.9 Hz, bipy); 8.01 (dd, 2H, *J* = 1.5 and 5.6 Hz, bipy); 8.12 (dd, 2H, *J* = 1.5 and 5.6 Hz, bipy); 8.16 (td, 2H, *J* = 1.5 and 7.9 Hz, bipy); 8.25 (td, 2H, *J* = 1.5 and 7.9 Hz, bipy); 8.40 (s, 2H, phen); 8.48 (d, 2H, *J* = 1.9 Hz, phen); 8.79 (d, 2H, *J* = 7.9 Hz, bipy); 8.83 (d, 2H, *J* = 7.9 Hz, bipy); 9.07 (d, 2H, *J* = 1.9 Hz, phen). ESMS: *m/z* = 376.0 [*M* – 2PF₆]²⁺. High resolution ESMS: *m/z* = 375.9650 (calculated for [C₃₂H₂₂N₆Br₂Ru]²⁺, 375.9648).

Compound Ru•E. A mixture of compound **A** (0.53 g, 0.55 mmol), (dppf)PdCl₂.CH₂Cl₂ (0.05 g, 0.06 mmol) and CuI (0.01 g, 0.05 mmol) in anhydrous DMF / ⁱPr₂NH (6 cm³, 5:1, v:v)

was deoxygenated with argon for 30 minutes. To this was added dropwise a solution of compound **C** (0.62 g, 1.00 mmol) in deoxygenated anhydrous DMF / $i\text{Pr}_2\text{NH}$ (3 cm³, 5:1, v:v). The solution was stirred at room temperature for 16 hours under argon, before removal of the solvent under reduced pressure. The resulting brown solid was purified by column chromatography on silica gel (200-300 mesh) with CH₃CN/H₂O/sat. KNO_{3(aq)} (100:0:0 to 100:4:2, v:v:v) as the eluent. The solvent was then removed under reduced pressure and the solid dissolved in CH₂Cl₂ (30 cm³), washed with an excess of saturated KPF_{6(aq)} solution (20 cm³) and separated. The aqueous layer was extracted with further portions of CH₂Cl₂ (2 x 15 cm³) and the combined organic layers then washed with water (2 x 15 cm³) and dried (MgSO₄). The solvent was removed under reduced pressure to afford complex **Ru•E** (0.41 g, 50 %) as a dark red solid. ¹H NMR (400 MHz, d₆-acetone): δ = 1.45 (s, 36H, ^tBu); 3.49 (s, 8H, N-CH₂-ester); 4.00 (s, 4H, CH₂-pyridyl); 7.37-7.45 (m, 2H, bipy); 7.61 (s, 2H, pyridyl H³/H⁵); 7.62-7.67 (m, 2H, bipy); 7.88 (d, 1H, J = 5.6 Hz, bipy); 7.96 (dd, 1H, J = 5.2 and 8.2 Hz, phen); 8.09 (d, 1H, J = 5.6 Hz, bipy); 8.13 (d, 1H, J = 5.6 Hz, bipy); 8.14-8.20 (m, 2H, bipy); 8.21 (d, 1H, J = 5.6 Hz, bipy); 8.26 (t, 2H, J = 7.9 Hz, bipy); 8.40-8.50 (m, 3H, phen); 8.67 (d, 1H, J = 1.9 Hz, phen); 8.79-8.88 (m, 5H, 4 x bipy, 1 x phen); 9.04 (d, 1H, J = 1.9 Hz, phen). ESMS: m/z = 604.7 [$M - 2\text{PF}_6$]²⁺. High resolution ESMS: m/z = 604.7318 (calculated for [C₆₅H₇₃N₉O₈Ru]²⁺, 604.7316).

Compound Ru•L. A solution of **Ru•E** (73 mg, 0.049 mmol) in CH₂Cl₂ (3 cm³) and trifluoroacetic acid (TFA, 3 cm³) was stirred at room temperature for 18 hours. The solvent was then removed under reduced pressure to yield a red solid. To remove any residual TFA the solid was dissolved in CH₂Cl₂ (10 cm³) and then evaporated to dryness *in vacuo*. This process was repeated ten times. The solid was then washed with CH₃OH (10 x 10 cm³) following the same procedure. Finally, the red solid was dissolved in the minimum amount of CH₃OH and precipitated with an excess of diethyl ether. The solid was collected by centrifugation and dried under a stream of N₂ to yield **Ru•L** (61 mg, 98 %) as a red solid. ¹H NMR (500 MHz, d₆-DMSO, 303 K): δ = 3.46 (s, 8H, N-CH₂-acid); 3.94 (s, 4H, CH₂-pyridyl); 7.33-7.38 (m, 2H, bipy); 7.53 (d, 1H, J = 5.3 Hz, bipy); 7.56 (s, 2H, pyridyl H³/H⁵); 7.56-7.62 (m, 2H, bipy); 7.75 (d, 2H, J = 5.3 Hz, bipy); 7.87 (d, 1H, J = 5.3 Hz, bipy); 7.90 (dd, 1H, J = 5.2 and 8.2 Hz, phen); 8.07-8.16 (m, 3H, 2 x bipy, 1 x phen); 8.21 (t, 2H, J = 7.8 Hz, bipy); 8.29 (d, 1H, J = 1.0 Hz, phen); 8.35 (d, 1H, J = 8.8 Hz, phen); 8.44 (d, 1H, J = 8.8 Hz, phen); 8.78-8.90 (m, 5H, 4 x bipy, 1 x phen); 9.16 (d, 1H, J = 1.0 Hz, phen). ESMS: m/z = 492.6 [$M - 2\text{PF}_6$]²⁺,

328.7 $[M - 2PF_6 + H]^{3+}$. High resolution ESMS: $m/z = 492.6056$ (calculated for $[C_{49}H_{41}N_9O_8Ru]^{2+}$, 492.6055).

Compound Ru•E₂. A mixture of compound **D** (1.02 g, 0.98 mmol), (dppf)PdCl₂.CH₂Cl₂ (0.05 g, 0.06 mmol) and CuI (0.01 g, 0.05 mmol) dissolved in anhydrous DMF / ⁱPr₂NH (6 cm³, 5:1, v:v) was deoxygenated with argon for 30 minutes. To this was added dropwise a solution of **C** (1.28 g, 2.07 mmol) in deoxygenated anhydrous DMF / ⁱPr₂NH (3 cm³, 5:1, v:v). The solution was stirred at room temperature for 16 hours under argon before the addition of an additional portion of **C** (1.28 g, 2.07 mmol) in the same deoxygenated solvent mixture. The reaction was stirred under argon for 24 hours before the solvent was removed under reduced pressure. The resulting brown solid was purified by column chromatography on silica gel (200-300 mesh) with CH₃CN/H₂O/sat. KNO_{3(aq)} (100:0:0 to 100:4:2, v:v:v) as the eluent. The solvent was then removed under reduced pressure and the solid dissolved in CH₂Cl₂ (30 cm³), washed with an excess of saturated KPF_{6(aq)} solution (20 cm³) and separated. The aqueous layer was extracted with further portions of CH₂Cl₂ (2 x 15 cm³) and the combined organic layers then washed with water (2 x 15 cm³), dried (MgSO₄) and the solvent removed under reduced pressure. Further purification was then achieved by size exclusion chromatography on Sephadex® LH-20 in CH₃OH. The solvent was removed under reduced pressure to afford **Ru•E₂** (0.94 g, 45 %) as a dark red solid. ¹H NMR (400 MHz, d₆-acetone): δ = 1.45 (br s, 72H, ^tBu); 3.49 (br s, 16H, N-CH₂-ester); 3.99 (br s, 8H, CH₂-pyridyl); 7.40-7.45 (m, 2H, bipy); 7.56 (s, 4H, pyridyl H³/H⁵); 7.60-7.66 (m, 2H, bipy); 8.05 (d, 2H, *J* = 5.6 Hz, bipy); 8.12-8.21 (m, 4H, bipy); 8.25 (t, 2H, *J* = 7.9 Hz, bipy); 8.48 (s, 2H, phen); 8.67 (d, 2H, *J* = 1.9 Hz, phen); 8.85 (m, 4H, bipy); 9.05 (d, 2H, *J* = 1.9 Hz, phen). ESMS: $m/z = 912.4$ $[M - 2PF_6]^{2+}$, 608.6 $[M - 2PF_6 + H]^{3+}$. High resolution ESMS: $m/z = 912.4073$ (calculated for $[C_{98}H_{122}N_{12}O_{16}Ru]^{2+}$, 912.4067).

Compound Ru•L₂. A solution of **Ru•E₂** (92 mg, 0.044 mmol) in CH₂Cl₂ (3 cm³) and TFA (3 cm³) was stirred at room temperature for 18 hours. The solvent was then removed under reduced pressure to yield a red solid. This was purified and isolated exactly as described for **Ru•L** (above) and dried under a stream of N₂ to yield **Ru•L₂** (71 mg, 98 %) as a red solid. ¹H NMR (400 MHz, D₂O): δ = 4.16 (br s, 16H, N-CH₂-acid); 4.74 (br s, 8H, CH₂-pyridyl); 7.17-7.31 (br m, 2H, bipy) 7.37-7.48 (br m, 2H, bipy); 7.65 (br d, 2H, *J* = 4.0 Hz, bipy); 7.69 (br s, 4H, pyridyl H³/H⁵); 7.90 (br d, 2H, *J* = 4.8 Hz, bipy); 7.98-8.06 (br m, 2H, bipy); 8.06-8.16 (br m, 2H, bipy); 8.25 (br s, 2H, phen); 8.35 (br s, 2H, phen); 8.51-8.63 (br m, 4H, bipy); 8.74 (br

s, 2H, phen). ESMS: $m/z = 688.2 [M - 2PF_6]^{2+}$. High resolution ESMS: $m/z = 688.1568$ (calculated for $[C_{66}H_{58}N_{12}O_{16}Ru]^{2+}$, 688.1563).

Compound Ru•Gd. To a solution of **Ru•L** (45 mg, 0.035 mmol) in water (3 cm³) at 0 °C was added dropwise a solution of GdCl₃·6H₂O (14 mg, 0.038 mmol) in water (0.5 cm³); the mixture was stirred and allowed to reach room temperature. After 1 hour the solution was adjusted to pH 5-6 using a solution of NaOH_(aq) (1M) and was then left to stir at room temperature for a further 18 hours. Saturated KPF_{6(aq)} solution was then added to produce a red precipitate (hexafluorophosphate salt of mono-cationic **Ru•Gd**) which was filtered and washed with water. This red solid was dissolved in the minimum amount of CH₃OH and precipitated with an excess of diethyl ether. The precipitate was collected by centrifugation and purified further using Sephadex® LH-20 with CH₃OH. The solvent was removed under reduced pressure and the resulting red solid dried under a stream of N₂. Counterion exchange was then achieved using Dowex® 1x2 chloride form (100-200 mesh) in water. The aqueous solution was filtered, the water removed under reduced pressure, and the resulting solid dried under a stream of N₂ to yield **Ru•Gd** (chloride salt; 35 mg, 84 %) as a red solid. ESMS: $m/z = 570.1 [M - Cl + H]^{2+}$, 380.4 $[M - Cl + 2H]^{3+}$. High resolution ESMS: $m/z = 570.0562$ (calculated for $[C_{49}H_{37}N_9O_8RuGd + H]^{2+}$, 570.0558).

Compound Ru•Gd₂ was prepared using the same method as described above for **Ru•Gd**, from **Ru•L₂** (100 mg, 0.060 mmol) and GdCl₃·6H₂O (59 mg, 0.159 mmol) in water, but without the counter-ion exchange step as **Ru•Gd₂** is neutral. At the end of the reaction the solution was purified by chromatography on Sephadex® LH-20 with water. Evaporation of the solvent afforded **Ru•Gd₂** (70 mg, 69 % yield) as a red solid. ESMS: $m/z = 842.1 [M + 2H]^{2+}$, 852.5 $[M + Na + H]^{2+}$, 864.6 $[M + 2Na]^{2+}$. High resolution ESMS: $m/z = 842.5664$ (calculated for $[C_{66}H_{50}N_{12}O_{16}RuGd_2 + 2H]^{2+}$, 842.5530).

Compound Ru•Nd. A solution of **Ru•L** (15 mg, 0.012 mmol) in water (3 cm³) was adjusted to pH 5-6 using NaOH_(aq) (0.1 M). With stirring, a solution of Nd(OTf)₃ (11 mg, 0.019 mmol) in water (0.5 cm³) was added dropwise. The mixture was stirred at room temperature and the pH readjusted to 5-6 using NaOH_(aq) (0.1 M) when necessary. After 18 hours, a small portion of Dowex® 1x2 chloride form (100-200 mesh) was added and the mixture stirred at room temperature for a further 24 hours. The solution was then filtered, concentrated under reduced pressure and purified on Sephadex® G-15 eluting with water. The solvent was removed under reduced pressure and the resulting solid dried under a

stream of N₂ to yield **Ru•Nd** (chloride salt; 13 mg, 95 %) as a red solid. ESMS: $m/z = 563.0$ [$M - Cl + H$]²⁺, 375.7 [$M - Cl + 2H$]³⁺. High resolution ESMS: $m/z = 563.0497$ (calculated for [C₄₉H₃₇N₉O₈¹⁰²Ru¹⁴⁴Nd + H]²⁺, 563.0488).

Compound Ru•Yb was prepared in exactly the same way as **Ru•Nd**, with **Ru•L** (18 mg, 0.014 mmol) and Yb(OTf)₃ (14 mg, 0.023 mmol) affording 14 mg (83 % yield) of **Ru•Yb** as a red solid. ESMS: $m/z = 578.1$ [$M - Cl + H$]²⁺. High resolution ESMS: $m/z = 578.0632$ (calculated for [C₄₉H₃₇N₉O₈¹⁰²Ru¹⁷³Yb + H]²⁺, 578.0632).

Compound Ru•Nd₂ was prepared in the same way as for **Ru•Gd₂**, with **Ru•L₂** (11.4 mg, 0.007 mmol) and Nd(OTf)₃ (10 mg, 0.017 mmol) affording 11 mg (97 % yield) of **Ru•Nd₂** as a red solid after purification on Sephadex® G-15 eluting with water. ESMS: $m/z = 829.0$ [$M + 2H$]²⁺, 553.0 [$M + 3H$]³⁺, 415.0 [$M + 4H$]⁴⁺. High resolution ESMS: $m/z = 829.0404$ (calculated for [C₆₆H₅₀N₁₂O₁₆¹⁰²Ru¹⁴⁴Nd₂ + 2H]²⁺, 829.0429).

Compound Ru•Yb₂ was prepared in the same way as for **Ru•Gd₂**, with **Ru•L₂** (7.4 mg, 0.004 mmol) and Yb(OTf)₃ (7 mg, 0.011 mmol) affording 7.5 mg (99 % yield) of **Ru•Yb₂** after purification on Sephadex® G-15 eluting with water. ESMS: $m/z = 858.1$ [$M + 2H$]²⁺, 572.4 [$M + 3H$]³⁺, 429.5 [$M + 4H$]⁴⁺. High resolution ESMS: $m/z = 858.0683$ (calculated for [C₆₆H₅₀N₁₂O₁₆¹⁰²Ru¹⁷³Yb₂ + 2H]²⁺, 858.0710).

Compound Ru•Mn. To a stirred solution of **Ru•L** (130 mg, 0.102 mmol) in water (3 cm³), adjusted to pH 5 – 6 with NaOH_(aq), was added dropwise a solution of MnCl₂·4H₂O (26 mg, 0.131 mmol) in water (0.5 cm³). The mixture was stirred at room temperature and the pH re-adjusted to 5 – 6 if necessary. After 18 hours the reaction mixture was concentrated under reduced pressure and purified on Sephadex® G-15, eluting with water. The solvent was removed under reduced pressure and the resulting red solid dried under a stream of N₂ to yield **Ru•Mn** (100 mg, 95 %) as a red solid. ESMS: $m/z = 519.1$ [$M + 2H$]²⁺. High resolution ESMS: $m/z = 519.0658$ (calculated for [C₄₉H₃₇N₉O₈RuMn + 2H]²⁺, 519.0674).

Compound Ru•Zn. This was prepared in exactly the same way as **Ru•Mn**, from **Ru•L** (38 mg, 0.03 mmol) and ZnCl₂·xH₂O (10 mg, *ca.* 0.049 mmol) to give **Ru•Zn** (25 mg, 80 %) as a red solid. ¹H NMR (400 MHz, D₂O): δ = 3.34-3.52 (m, 8H, NCH₂-CO₂); 4.15 (s, 4H, NCH₂-pyridyl); 7.16-7.26 (m, 2H, bipy); 7.39-7.46 (m, 2H, bipy); 7.48 (s, 1H, pyridyl H³ or H⁵); 7.52 (s, 0.5H, pyridyl H³ or H⁵); 7.54 (s, 0.5H, pyridyl H³ or H⁵); 7.58 (d, 1H, *J* = 5.3 Hz, bipy); 7.68 (d, 1H, *J* = 5.3 Hz, bipy); 7.73 (t, 1H, *J* = 6.5 Hz, phen); 7.91 (d, 1H, *J* = 5.3 Hz, bipy); 7.94 (d, 1H, *J* = 5.3 Hz, bipy); 7.99 (t, 2H, *J* = 7.5 Hz, bipy); 8.09 (t, 2H, *J* = 7.5 Hz, bipy); 8.18 (d, 1H, *J* =

4.8 Hz, phen); 8.19-8.29 (m, 2H, phen); 8.35 (d, 1H, $J = 4.5$ Hz, phen); 8.50-8.64 (m, 5H, 4 x bipy, 1 x phen); 8.76 (s, 0.5H, phen); 8.79 (s, 0.5H, phen). ESMS: $m/z = 523.6 [M + 2H]^{2+}$. High resolution ESMS: $m/z = 523.5632$ (calculated for $[C_{49}H_{37}N_9O_8RuMn + 2H]^{2+}$, 523.5626).

Compound Ru•Mn₂. This was prepared in the same way as **Ru•Mn**, from **Ru•L₂** (41 mg, 0.025 mmol) and $MnCl_2 \cdot 4H_2O$ (12 mg, 0.061 mmol), affording after purification (Sephadex® G-15, eluting with water) pure **Ru•Mn₂** as its disodium salt (25 mg, 67 %). ESMS: $m/z = 739.1 [M - 2Na]^{2-}$. High resolution ESMS: $m/z = 739.0598$ (calculated for $[C_{66}H_{50}N_{12}O_{16}^{102}RuMn_2]^{2-}$, 739.0631).

Compound Ru•Zn₂. This was prepared in the same way as **Ru•Zn**, from **Ru•L₂** (9 mg, 5.2 μ mol) and $ZnCl_2 \cdot xH_2O$ (10 mg, *ca.* 49 μ mol), affording after purification (Sephadex® G-15, eluting with water) pure **Ru•Zn₂** as its disodium salt (7 mg, 82 %). ESMS: $m/z = 748.1 [M - 2Na]^{2-}$. High resolution ESMS: $m/z = 748.0532$ (calculated for $[C_{66}H_{50}N_{12}O_{16}^{102}Ru^{64}Zn_2]^{2-}$, 748.0553).

Computational Details

All calculations were performed with Gaussian 09 v. D.01²⁸ using density-functional theory. The functional used was B3LYP²⁹ with empirical dispersion corrections through the GD3BJ keyword.³⁰ The basis set used consisted of SDD³¹ on Ru or lanthanide atoms, and 6-311G(d,p)^{32,33} on all other atoms. All bulk solvent was described using the PCM method^{34,35} as implemented in Gaussian using the provided parameters for water. No additional water molecules were included to simulate hydrogen bonding.

All **Ru•Mn** complexes (and their reduced/oxidized forms) were assumed to be in the high-spin configuration for Mn, where relevant. During the calculations it was found that there is a large manifold of potential sextet states for **Ru•Mn**. Different starting geometries will lead to different final electronic states for a similar final geometry with the pyridine fragment of the Mn(II) moiety co-planar with the phen fragment of the Ru(II) moiety. In fact, the lowest sextet energies were obtained by starting from a geometry in which the pyridine fragment of the Mn(II) moiety is perpendicular to the phen fragment of the Ru(II) fragment, i.e. through restricting the size of the conjugated system. Coupling between the excited-state (³MLCT) Ru(II) and ground-state Mn(II) moieties was assumed to be weakly anti-ferromagnetic upon excitation: preliminary calculations on the octet state (which would arise from ferromagnetic coupling) of photo-excited **Ru•Mn** all show a higher energy than

the corresponding quartet states. For all optimised structures frequencies were calculated in the harmonic approximation. Only small imaginary frequencies ($< 15 \text{ cm}^{-1}$) were found. These molecules were considered to be true minima, since such small imaginary values are commonly associated with errors in the integration grids used.

All absorption spectra were calculated with the TD-DFT method³⁶ as implemented in G09. All images were created with in-house developed software, which is available upon request. The overlays were created using ROCS.^{37,38} Finally, the computational ESI was created using in-house developed software based on the Open Eye Toolkit.³⁹

Acknowledgements. We thank the University of Sheffield (Ph.D studentships to BJC, AJA); the EPSRC Capital Equipment award for the Lord Porter laser laboratory in Sheffield (EP/L022613/1), the Grantham Center for Sustainable Futures (Ph.D studentship to JDS) and The Rosetrees Trust (Ph.D studentship to CJ). We also gratefully acknowledge (i) the use of the Wolfson Light Microscopy Facility at the University of Sheffield, and (ii) a license for the OpenEye tools, obtained *via* the free academic licensing program.

References

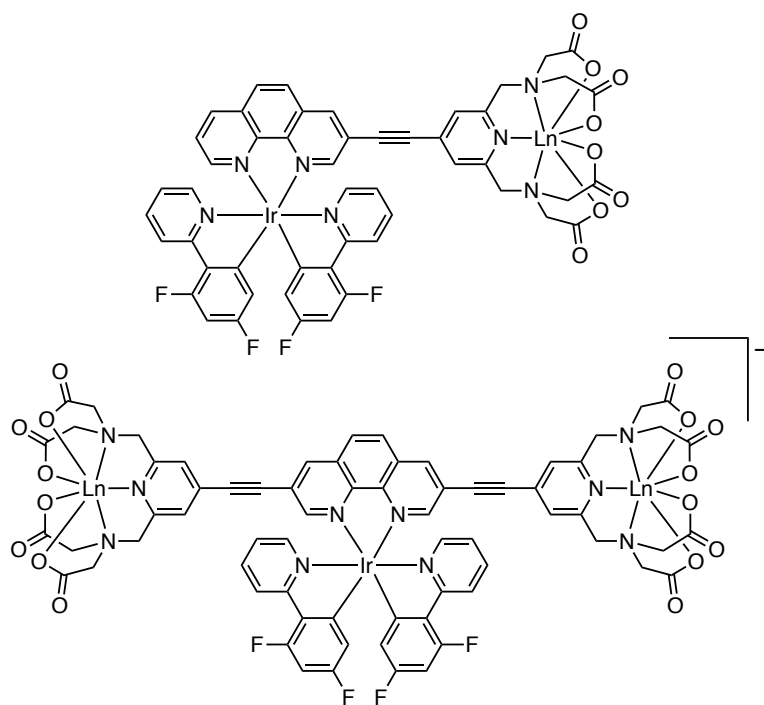
- 1 (a) M. D. Ward, *Coord. Chem. Rev.*, 2007, **251**, 1663; (b) L. Aboshyan-Sorgho, M. Cantuel, S. Petoud, A. Hauser and C. Piguet, *Coord. Chem. Rev.*, 2012, **256**, 1644; (c) L.-J. Xu, G.-T. Xu and Z.-N. Chen, *Coord. Chem. Rev.*, 2014, **273-274**, 47; (d) C. E. Plečnik, S. Liu and S. G. Shore, *Acc. Chem. Res.*, 2003, **36**, 499; (e) A. Chakraborty, J. Goura, P. Kalita, A. Swain, G. Rajaraman and V. Chandrasekhar, *Dalton Trans.*, 2018, **47**, 8841; (f) K. Liua, W. Shi and P. Chenga, *Coord. Chem. Rev.*, 2015, **289-290**, 74.
- 2 (a) P. Coppo, M. Duati, V. N. Kozhevnikov, J. W. Hofstraat and L. De Cola, *Angew. Chem., Int. Ed. Engl.*, 2005, **44**, 1806; (b) D. Sykes, I. S. Tidmarsh, A. Barbieri, I.V. Sazanovich, J. A. Weinstein and M. D. Ward, *Inorg. Chem.*, 2011, **50**, 11323; (c) G. Yu, Y. Xing, F. Chen, R. Han, J. Wang, Z. Bian, L. Fu, Z. Liu, X. Ai, J. Zhang and C. Huang, *ChemPlusChem*, 2013, **78**, 852; (d) D. Sykes, A. J. Cankut, N. Mohd Ali, A. Stephenson, S. J. P. Spall, S. C. Parker, J. A. Weinstein and M. D. Ward, *Dalton Trans.*, 2013, **43**, 6414.
- 3 (a) T. Lazarides, D. Sykes, S. Faulkner, A. Barbieri and M. D. Ward, *Chem. Eur. J.*, 2008, **14**, 9389; (b) T. Lazarides, N. M. Tart, D. Sykes, S. Faulkner, A. Barbieri and M. D. Ward, *Dalton Trans.*, 2009, 3971; (c) S. Faulkner, L. S. Natrajan, W. S. Perry and D. Sykes, *Dalton Trans.*, 2009, 3890; (d) M. D. Ward, *Coord. Chem. Rev.*, 2010, **254**, 2634; (e) F.-F. Chen, Z.-Q. Chen, Z.-Q. Bian and C.-H. Huang, *Coord. Chem. Rev.*, 2010, **254**, 991.
- 4 (a) E. Debroye and T. N. Parac-Vogt, *Chem. Soc. Rev.*, 2014, **43**, 8178; (b) L. E. Jennings and N. J. Long, *Chem. Commun.*, 2009, 3511; (c) M. Tropiano, C. J. Record, E. Morris, H. S. Rai, C. Allain and S. Faulkner, *Organometallics*, 2012, **31**, 5673; (d) P. Verwilt, S. V. Eliseeva, L. Vander Elst, C. Burtea, S. Laurent, S. Petoud, R. N. Muller, T. N. Parac-Vogt and W. M. De Borggraeve, *Inorg. Chem.*, 2012, **51**, 6405; (e) P. Verwilt, S. Park, B. Yoon and J. S. Kim, *Chem. Soc. Rev.*, 2015, **44**, 1791; (f) T. Koullourou, L. Natrajan, H. Bhavsar, S. J. A. Pope, J. Feng, R. Kauppinen, J. Narvainen, R. Shaw, E. Scales, A. Kenwright and S. Faulkner, *J. Am. Chem. Soc.*, 2008, **130**, 2178; (g) A. Nithyakumar and V. Alexander, *New J. Chem.*, 2016, **40**, 4606; (h) A. Boulay, C. Deraeve, L. Vander Elst, N. Leygue, O. Maury, S. Laurent, R. N. Muller, B. Maestre-Voegtli and C. Picard, *Inorg. Chem.*, 2015, **54**, 1414.

- 5 E. Baggaley, D.-K. Cao, D. Sykes, S. W. Botchway, J. A. Weinstein and M. D. Ward, *Chem. Eur. J.*, 2014, **20**, 8898.
- 6 (a) A. Jana, E. Baggaley, A. Amoroso and M. D. Ward, *Chem. Commun.*, 2015, **51**, 8833; (b) A. Jana, B. J. Crowston, J. R. Shewring, L. K. McKenzie, H. E. Bryant, S. W. Botchway, A. D. Ward, A. J. Amoroso, E. Baggaley and M. D. Ward, *Inorg. Chem.*, 2016, **55**, 5623.
- 7 (a) M. R. Gill, J. Garcia-Lara, S. J. Foster, C. Smythe, G. Battaglia and J. A. Thomas, *Nat. Chem.*, 2009, **1**, 662; (b) E. Baggaley, M. R. Gill, N. H. Green, D. Turton, I. V. Sazanovich, S. W. Botchway, C. Smythe, J. W. Haycock, J. A. Weinstein and J. A. Thomas, *Angew. Chem., Int. Ed.*, 2014, **53**, 3367; (c) M. P. Coogan and V. Fernández-Moreira, *Chem. Commun.*, 2014, **50**, 384; (d) S. Zhang, Y. Ding and H. Wei, *Molecules*, 2014, **19**, 11933; (e) T. S.-M. Tang, H.-W. Liu and K. K.-W. Lo, *Chem. Eur. J.*, 2016, **22**, 9648; (f) E. Baggaley, J. A. Weinstein and J. A. G. Williams, *Struct. Bonding*, 2015, **165**, 205; (g) L. K. McKenzie, H. E. Bryant and J. A. Weinstein, *Coord. Chem. Rev.*, 2019, **379**, 2; (h) L. K. McKenzie, I. V. Sazanovich, E. Baggaley, M. Bonneau, V. Guerchais, J. A. G. Williams, J. A. Weinstein and H. E. Bryant, *Chem. Eur. J.*, 2017, **23**, 234; (i) A. M.-H. Yip and K. K.-W. Lo, *Coord. Chem. Rev.*, 2018, **361**, 138.
- 8 (a) D. Tzalis and Y. Tor, *J. Am. Chem. Soc.*, 1997, **119**, 852; (b) T. Ren, *Chem. Rev.*, 2008, **108**, 4185.
- 9 D. Tzalis, Y. Tor, F. Salviatore and S. J. Siegel, *Tetrahedron Lett.*, 1995, **36**, 3489.
- 10 H. Li, J. Tatlock, A. Linton, J. Gonzalez, T. Jewell, L. Patel, S. Ludlum, M. Drowns, S. V. Rahavendran, H. Skor, R. Hunter, S. T. Shi, K. J. Herlihy, H. Parge, M. Hickey, X. Yu, F. Chau, J. Nonomiya and C. Lewis, *J. Med. Chem.*, 2009, **52**, 1255.
- 11 J.-L. Chen, X. Wang, F. Yang, C. Cao, G. Otting and X.-C. Su, *Angew. Chem. Int. Ed.*, 2016, **55**, 13744.
- 12 H. Takalo, P. Pasanen, J. Kankare, K. Undheim, G. Wittman, L. Gera, M. Bartók, I. Pelczer and G. Dombi, *Acta Chem. Scand.*, 1988, **42b**, 373.
- 13 P. Caravan, *Chem. Soc. Rev.*, 2006, **35**, 512.
- 14 (a) D. Fornasiero, J. C. Bellen, R. J. Baker and B. E. Chatterton, *Invest. Radiol.*, 1987, **22**, 322; (b) S. Aime, P. L. Anelli, M. Botta, M. Brochetta, S. Canton, F. Fedeli, E. Gianolio and E. Terreno, *J. Biol. Inorg. Chem.*, 2002, **7**, 58; (c) E. M. Gale, J. Zhu and P. Caravan, *J. Am. Chem. Soc.*, 2013, **135**, 18600. (d) J. Wang, H. Wang, I. A. Ramsay, D.

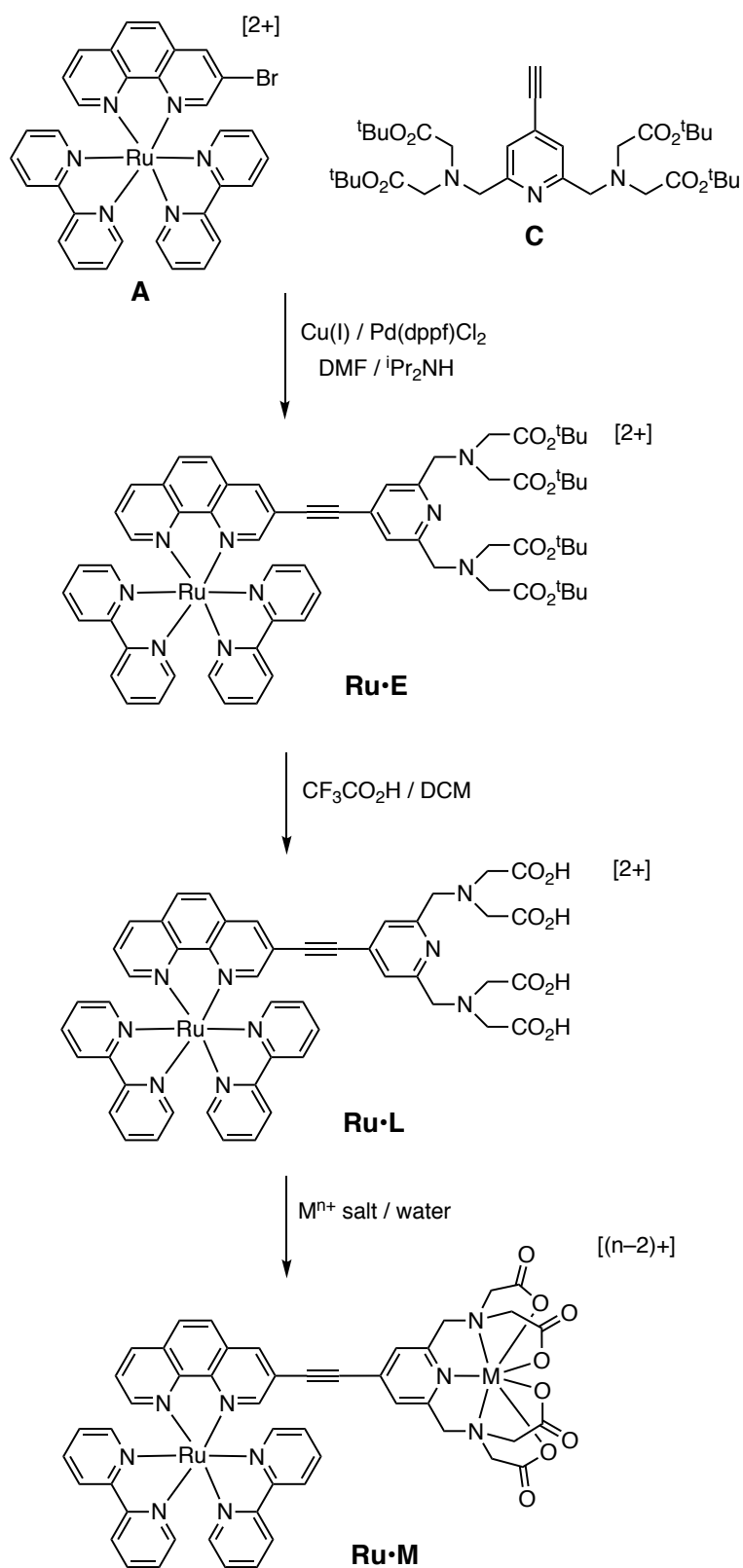
- J. Erstad, B. C. Fuchs, K. K. Tanabe, P. Caravan and E. M. Gale, *J. Med. Chem.*, 2018, **61**, 8811.
- 15 W. Shi, B. Song, W. Shi, X. Qin, Z. Liu, M. Tan, L. Wang, F. Song and J. Yuan, *ACS Appl. Mater. Interfaces*, 2018, **10**, 27681.
- 16 (a) A. Deroche, I. Morgenstern-Badarau, M. Cesario, J. Guilhem, B. Keita, L. Nadjio and C. Houée-Levin, *J. Am. Chem. Soc.*, 1996, **118**, 4567; (b) S. T. Frey, H. A. Ramirez, M. Kaur and J. P. Jasinski, *Acta Cryst. E, Cryst. Commun.*, 2018, **74**, 1075; (c) J. J. Stezowski, R. Countryman and J. L. Hoard, *Inorg. Chem.*, 1973, **12**, 1749; (d) G.-F. Liu, M. Filipović, F. W. Heinemann and I. Ivanovic-Burmazovic, *Inorg. Chem.*, 2007, **46**, 8825.
- 17 (a) S. M. Jahromi, M. Montazeri, A. Masoudiasl, E. Houshyar, S. Joohari and K. M. White, *Ultrasonics Sonochem.*, 2018, **41**, 590; (b) G. J. McManus, M. P. Perry, B. D. Wagner and M. J. Zaworotko, *J. Am. Chem. Soc.*, 2007, **129**, 9094; (c) P. Maheswari, B. Modéc, A. Pevec, B. Kozlevčar, C. Massera, P. Gamez and J. Reedijk, *Inorg. Chem.*, 2006, **45**, 6637.
- 18 A. Juris, V. Balzani, F. Barigelli and S. Campagna, *Coord. Chem. Rev.*, 1988, **84**, 85.
- 19 E. C. Glazer, D. Magde and Y. Tor, *J. Am. Chem. Soc.*, 2005, **127**, 4190.
- 20 M. D. Ward, *Coord. Chem. Rev.*, 2010, **254**, 2634.
- 21 W. DeW. Horrocks, Jr. and D. R. Sudnick, *J. Am. Chem. Soc.*, 1979, **101**, 334.
- 22 (a) N. M. Shavaleev, G. Accorsi, D. Virgili, Z. R. Bell, T. Lazarides, G. Calogero, N. Armaroli and M. D. Ward, *Inorg. Chem.*, 2005, **44**, 61; (b) N. M. Shavaleev, L. P. Moorcraft, S. J. A. Pope, Z. R. Bell, S. Faulkner and M. D. Ward, *Chem. Eur. J.*, 2003, **9**, 5283; (c) T. K. Ronson, T. Lazarides, H. Adams, S. J. A. Pope, D. Sykes, S. Faulkner, S. J. Coles, M. B. Hursthouse, W. Clegg, R. W. Harrington and M. D. Ward, *Chem. Eur. J.*, 2006, **12**, 9299.
- 23 (a) K. E. Berg, A. Tran, M. K. Raymond, M. Abrahamsson, J. Wolny, S. Redon, M. Andersson, L. Sun, S. Styring, L. Hammarström, H. Toftlund and B. Åkermark, *Eur. J. Inorg. Chem.*, 2001, 1019; (b) L. Sun, H. Berglund, R. Davydov, T. Norrby, L. Hammarström, P. Korall, A. Börje, C. Philouze, K. Berg, A. Tran, M. Andersson, G. Stenhagen, J. Mårtensson, M. Almgren, S. Styring and B. Åkermark, *J. Am. Chem. Soc.*, 1997, **119**, 6996; (c) M. L. A. Abrahamsson, H. B. Baudin, A. Tran, C. Philouze, K. E. Berg, M. K. Raymond-Johansson, L. Sun, B. Åkermark, S. Styring and L.

- Hammarström, *Inorg. Chem.*, 2002, **41**, 1534; (d) A. G. Tebo, S. Das, R. Farran, C. Herrero, A. Quaranta, R. Fallahpour, S. Protti, M.-F. Charlot and W. Leibl, *Comptes Rendus Chim.*, 2017, **20**, 323.
- 24 H. Berglund-Baudin, L. Sun, R. Davidov, M. Sundahl, S. Styring, B. Åkermark, M. Almgren and L. Hammarström, *J. Phys. Chem. A*, 1998, **102**, 2512.
- 25 S. Zális, C. Consani, A. El Nahhas, A. Cannizzo, M. Chergui, F. Hartl and A. Vlček, *Inorg. Chim. Acta*, 2011, **374**, 578.
- 26 B. P. Sullivan, D. J. Salmon and T. J. Meyer, *Inorg. Chem.*, 1978, **17**, 3334.
- 27 J. J. Snellenburg, S.P. Liptonok, R. Seger, K. M. Mullen and I. H. M. van Stokkum, *J. Stat. Soft.*, 2012, **49**, 1.
- 28 Gaussian 09, Revision D.01: M. J. Frisch, G. W. Trucks, H. B. Schlegel, G. E. Scuseria, M. A. Robb, J. R. Cheeseman, G. Scalmani, V. Barone, B. Mennucci, G. A. Petersson, H. Nakatsuji, M. Caricato, X. Li, H. P. Hratchian, A. F. Izmaylov, J. Bloino, G. Zheng, J. L. Sonnenberg, M. Hada, M. Ehara, K. Toyota, R. Fukuda, J. Hasegawa, M. Ishida, T. Nakajima, Y. Honda, O. Kitao, H. Nakai, T. Vreven, J. A. Montgomery, Jr., J. E. Peralta, F. Ogliaro, M. Bearpark, J. J. Heyd, E. Brothers, K. N. Kudin, V. N. Staroverov, T. Keith, R. Kobayashi, J. Normand, K. Raghavachari, A. Rendell, J. C. Burant, S. S. Iyengar, J. Tomasi, M. Cossi, N. Rega, J. M. Millam, M. Klene, J. E. Knox, J. B. Cross, V. Bakken, C. Adamo, J. Jaramillo, R. Gomperts, R. E. Stratmann, O. Yazyev, A. J. Austin, R. Cammi, C. Pomelli, J. W. Ochterski, R. L. Martin, K. Morokuma, V. G. Zakrzewski, G. A. Voth, P. Salvador, J. J. Dannenberg, S. Dapprich, A. D. Daniels, O. Farkas, J. B. Foresman, J. V. Ortiz, J. Cioslowski and D. J. Fox, Gaussian, Inc., Wallingford CT, 2013.
- 29 A. D. Becke, *J. Chem. Phys.*, 1993, **98**, 5648.
- 30 S. Grimme, S. Ehrlich and L. Goerigk, *J. Comput. Chem.*, 2011, **32**, 1456.
- 31 M. Dolg, U. Wedig, H. Stoll and H. Preuss, *J. Chem. Phys.*, 1987, **86**, 866.
- 32 A. D. McLean and G. S. Chandler, *J. Chem. Phys.*, 1980, **72**, 5639.
- 33 R. Krishnan, J. S. Binkley, R. Seeger and J. A. Pople, *J. Chem. Phys.*, 1980, **72**, 650.
- 34 M. Cossi, N. Rega, G. Scalmani and V. Barone, *J. Comput. Chem.*, 2003, **24**, 669.
- 35 J. Tomasi, B. Mennucci, R. Cammi, *Chem. Rev.*, 2005, **105**, 2999.
- 36 G. Scalmani, M. J. Frisch, B. Mennucci, J. Tomasi, R. Cammi, and V. Barone, *J. Chem. Phys.*, 2006, **124**, 094107
- 37 P. C. D. Hawkins, A. G. Skillman, A. Nicholls, *J. Med. Chem.*, 2007, **50**, 74.

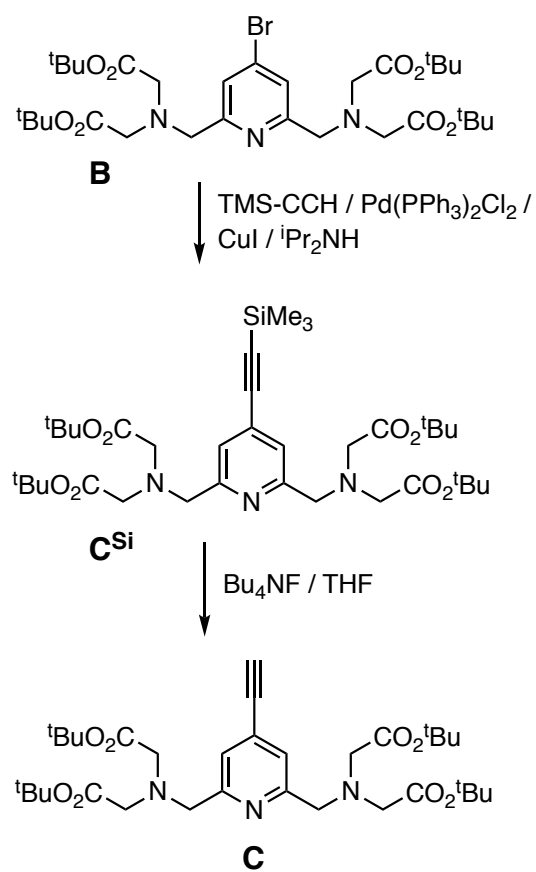
- 38 ROCS 3.2.2.2: OpenEye Scientific Software, Santa Fe, NM.
[http://www.eyesopen.com.](http://www.eyesopen.com)
- 39 OpenEye toolkits 2018.feb.1, OpenEye Scientific software, Santa Fe, NM.
[http://www.eyesopen.com.](http://www.eyesopen.com)



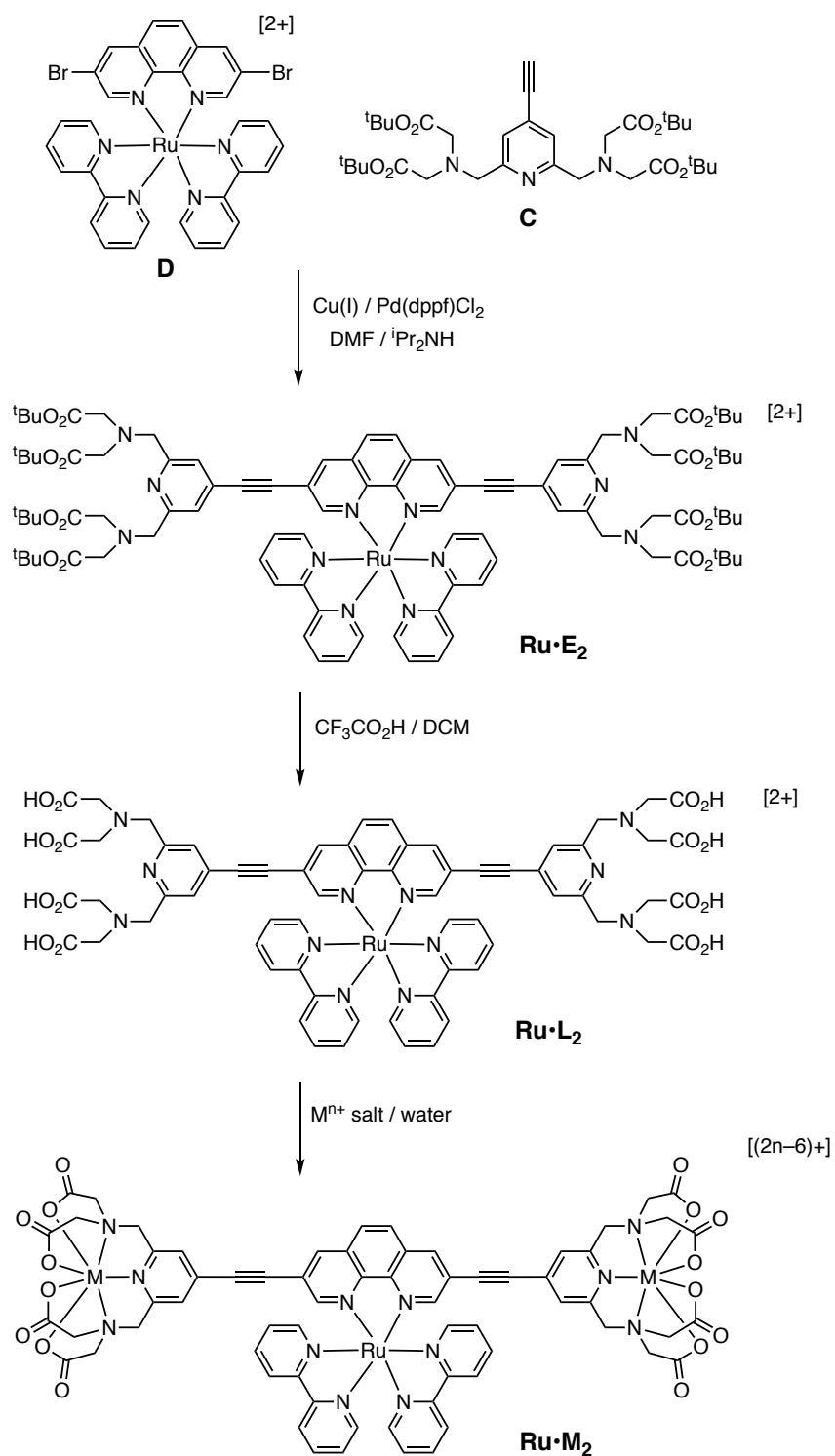
Scheme 1: Previously-reported Ir(III)/Ln(III) complexes based on a bridging ligand skeleton combining phenanthroline and polyaminocarboxylate binding sites for the Ir(III) and Ln(III) metal centres, respectively, connected by an alkyne spacer (see ref. 6).



Scheme 2. Preparation of **Ru•E**, **Ru•L** and heterodinuclear complexes **Ru•M**.



Scheme 3. Preparation of ester-protected alkyne intermediate **C** (used in Schemes 2 and 4)



Scheme 4. Preparation of **Ru•E₂**, **Ru•L₂** and heterotrimeric complexes **Ru•M₂**.

Table 1. UV/Vis absorption and luminescence data for the new mononuclear Ru(II) complexes.

	$\lambda_{\text{abs}}^{\text{RT}} / \text{nm}$ [$10^3 \epsilon / \text{M}^{-1} \text{cm}^{-1}$] ^a	$\lambda_{\text{em}}^{\text{RT}} / \text{nm}$ [τ / ns] ^a	$\lambda_{\text{em}}^{77\text{K}} / \text{nm}$ [$\tau / \mu\text{s}$] ^b
Ru•E	286 [88], 321 (sh) [39], 444 (br) [14]	647 [240]	611, 660 (sh), 711(sh) [6.2]
Ru•L	285 [120], 325 (sh) [55], 442 (br) [16]	661 [340]	611, 662 (sh), 706 (sh) [5.8]
Ru•E₂	351 [56], 437 [14], 476 (sh) [10].	683 [271]	645, 701 (sh) [3.8]
Ru•L₂	349 [46], 434 [6.5], 485 (sh) [3.7]	697 [209, 102]	<i>Not soluble</i>

a Absorption and emission spectra at RT measured in MeCN (**Ru•E** and **Ru•E₂**) or water (**Ru•L** and **Ru•L₂**). Estimated uncertainty in lifetimes is $\pm 10\%$ for single component decays.

b Emission spectra at 77 K measured in EtOH/MeOH (4:1, v/v) glass

Table 2. UV/Vis absorption and luminescence data for the Ru/M heterometallic complexes (M = Gd, Mn, Zn).

	$\lambda_{\text{abs}}^{\text{RT}} / \text{nm}$ [$10^3 \varepsilon / \text{M}^{-1} \text{cm}^{-1}$] ^a	$\lambda_{\text{em}}^{\text{RT}} / \text{nm}$ [τ / ns] ^a	$\lambda_{\text{em}}^{77\text{K}} / \text{nm}$ [$\tau / \mu\text{s}$] ^b
Ru•Gd	286 [56], 326 (sh) [25], 443 (br) [7.5]	664 [351]	612, 662 (sh), 706 (sh) [5.3]
Ru•Gd₂	286 [99], 350 [74], 435 [11], 486 (sh) [5.9]	699 [402, 104]	<i>not soluble</i>
Ru•Mn	285 [80], 325 (sh) [34], 441 (br) [10]	657 [410, 91]	612, 660, 709 [1.8, 0.45]
Ru•Mn₂	286 [86], 350 [59], 435 [7.9], 481 (sh) [4.4]	700 [456, 164, 21]	<i>not soluble</i>
Ru•Zn	285 [80], 326 (sh) [34], 440 (br) [10]	666 [329]	617, 668, 720 [5.6]
Ru•Zn₂	285 [88], 348 [55], 435 [9.2], 478 (sh) [5.3]	695 [301, 117]	<i>not soluble</i>

a Absorption and emission spectra at RT measured in water. Estimated uncertainty in lifetimes is $\pm 10\%$ for single component decays.

b Emission spectra at 77 K measured in EtOH/MeOH (4:1, v/v) glass.

Table 3. Luminescence data for the Ru/Yb and Ru/Nd heterometallic complexes.

	$\lambda_{\text{em}}^{\text{RT}} / \text{nm} [\tau / \text{ns}]$ in H_2O for Ru(II) emission ^a	$\lambda_{\text{em}}^{\text{RT}} / \text{nm} [\tau / \mu\text{s}]$ in D_2O for Ln(III) emission
Ru•Yb	663 [242, 73]	980 [13]
Ru•Yb₂	700 [223, 88]	980 [10.5, 0.3] ^b
Ru•Nd	662 [358, 22]	1060, 1380 [0.8]
Ru•Nd₂	703 [408, 18]	1060, 1380 [0.7]

a Two Ru(II)-based luminescence components: the shorter one is assumed to be associated with maximum quenching by the lanthanide (see main text).

b The shorter luminescence component detected at 980 nm is from the tail of unquenched Ru(II)-based emission which overlaps with the Yb(III)-based emission.

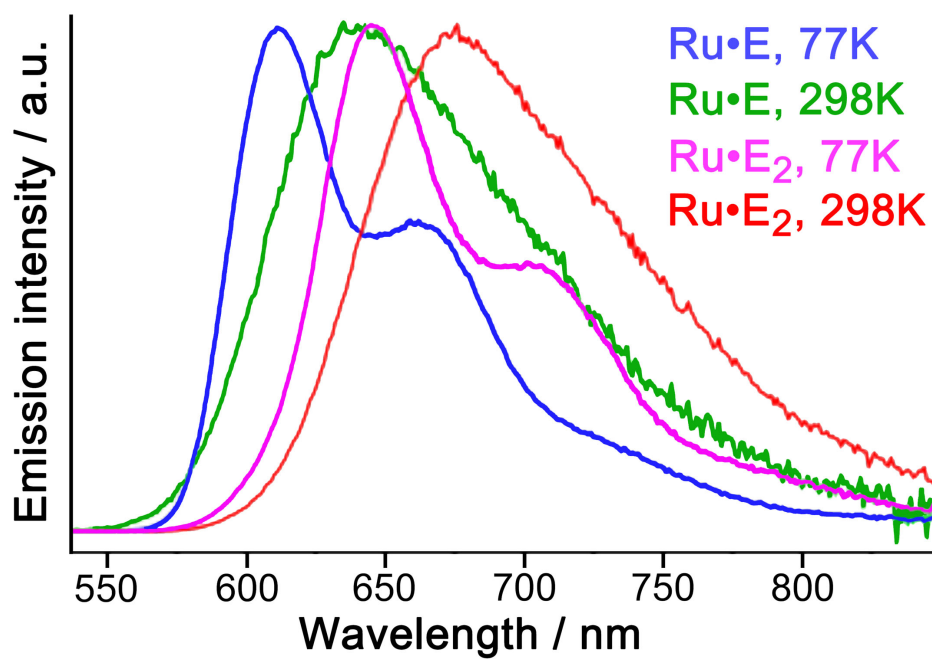


Fig. 1. Normalised, corrected luminescence spectra of the four mononuclear Ru(II) complexes in aerated EtOH/MeOH (4:1, v/v) at 298 K and in a glass at 77 K, excitation wavelength 435 nm.

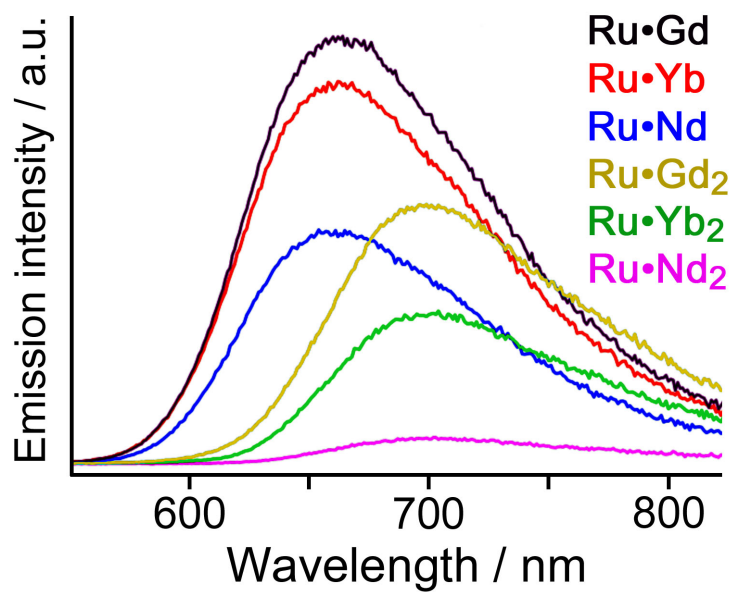


Fig. 2. Corrected luminescence spectra in water at RT showing the Ru(II)-based luminescence of the three dinuclear **Ru•Ln** and three trinuclear **Ru•Ln₂** complexes (Ln = Gd, Yb, Nd); all solutions were isoabsorbing at the excitation wavelength (λ_{exc} = 430 nm).

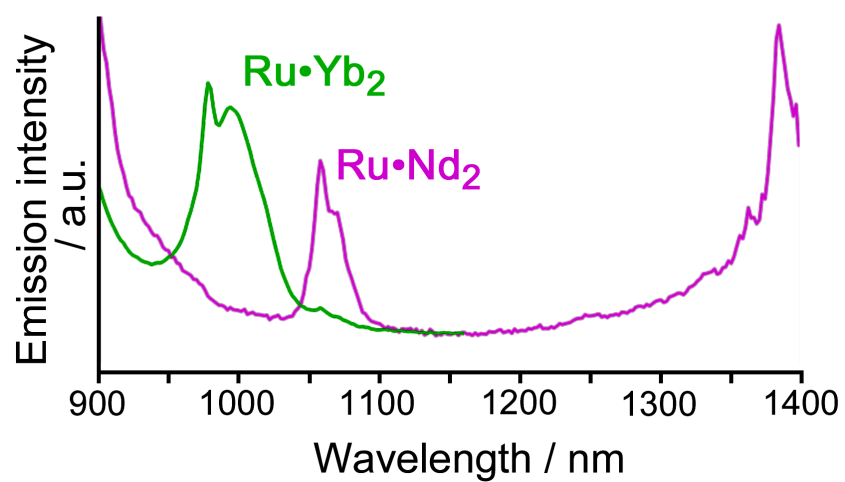


Fig. 3. Corrected luminescence spectra in D₂O at 298 K in the near-infrared region, showing the sensitised lanthanide-based luminescence from the complexes **Ru•Yb₂** and **Ru•Nd₂** complexes ($\lambda_{\text{exc}} = 440$ nm for both spectra).

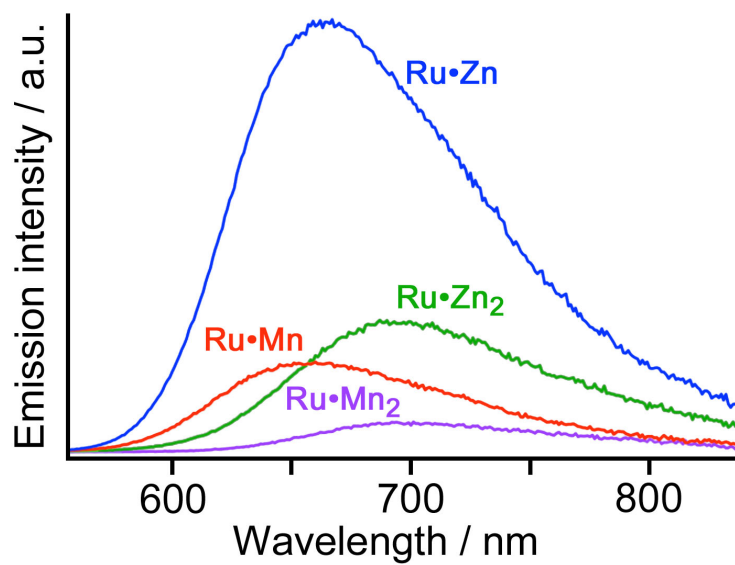


Fig. 4. Corrected luminescence spectra in water at 298 K for the four Ru/Mn and Ru/Zn complexes; all solutions were isoabsorbing at the excitation wavelength ($\lambda_{\text{exc}} = 435$ nm).

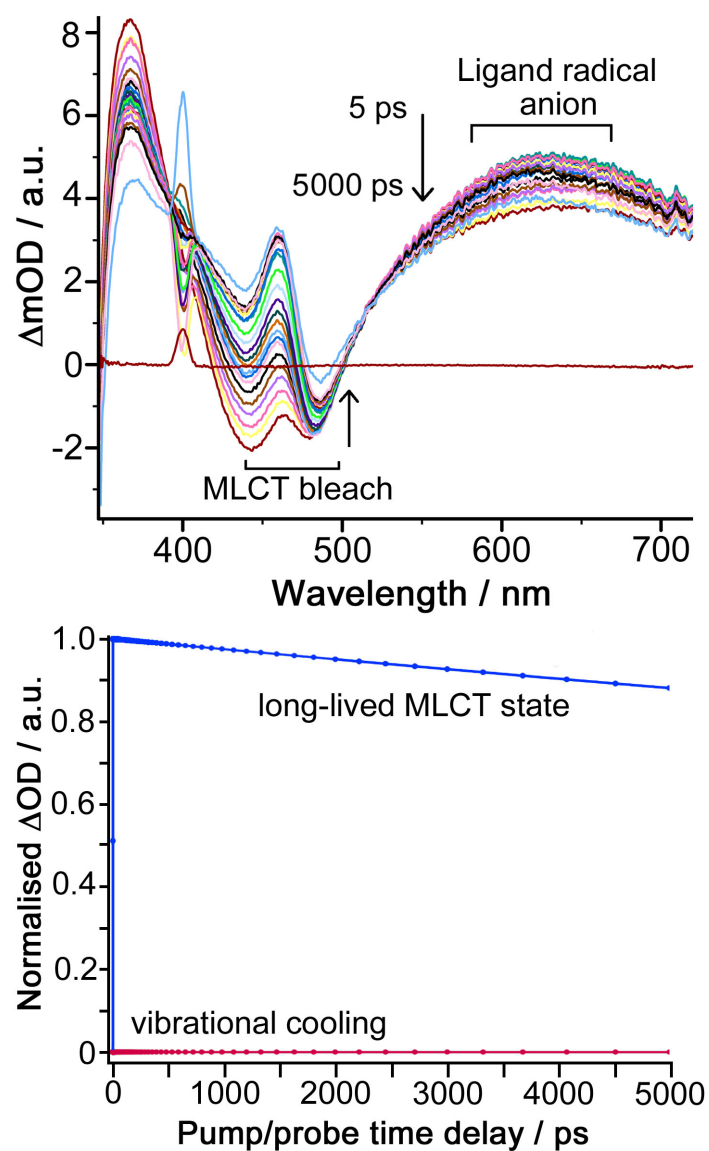


Fig. 5. Top: differential transient absorption spectra in air-equilibrated water of **Ru•Zn** at a range of different time delays following excitation ($\lambda_{\text{exc}} = 400 \text{ nm}$, 40 fs, 3 mW pulse). Bottom: dynamics of the transient signals over a 5 ns period.

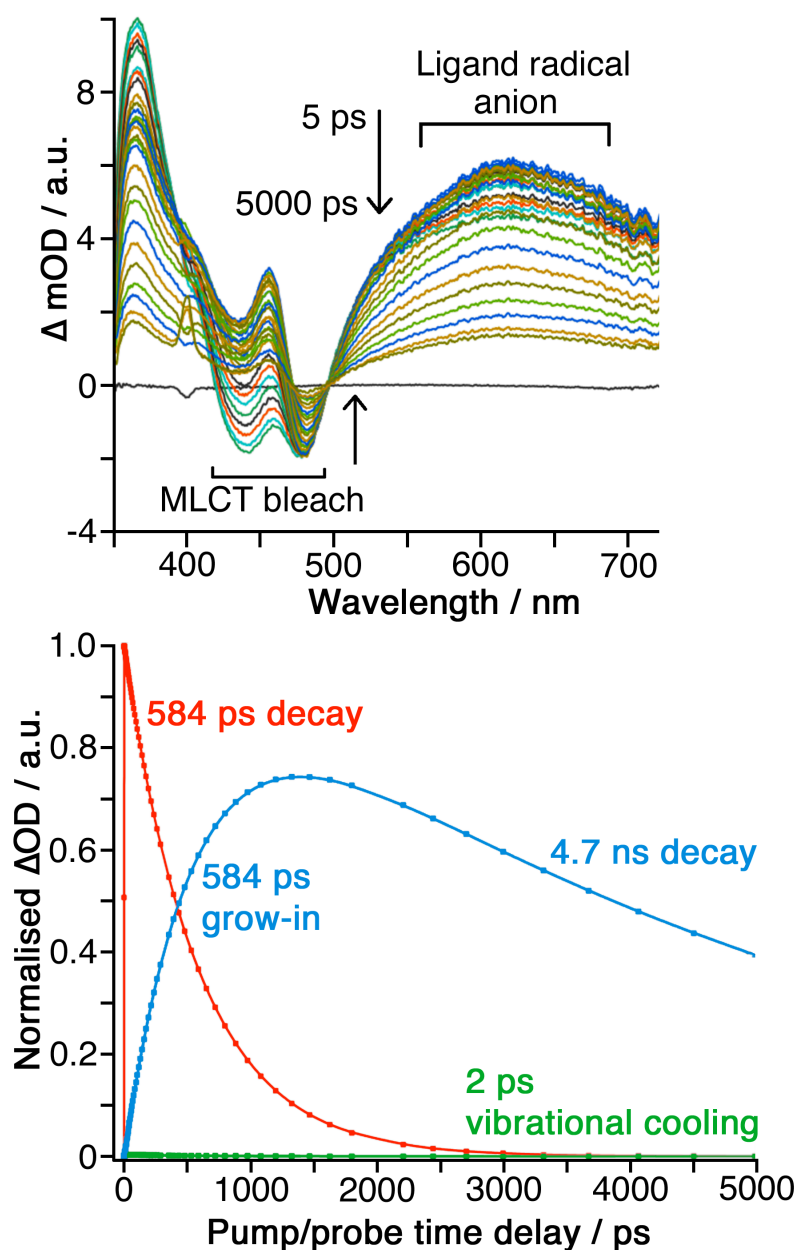


Fig. 6. Top: differential transient absorption spectra in air-equilibrated water of **Ru•Mn** at a range of different time delays following excitation ($\lambda_{exc} = 400$ nm, 40 fs, 3 mW pulse). The small sharp feature at 400 nm is scattering of the pump light. Bottom: dynamics of the transient signals over a 5 ns period.

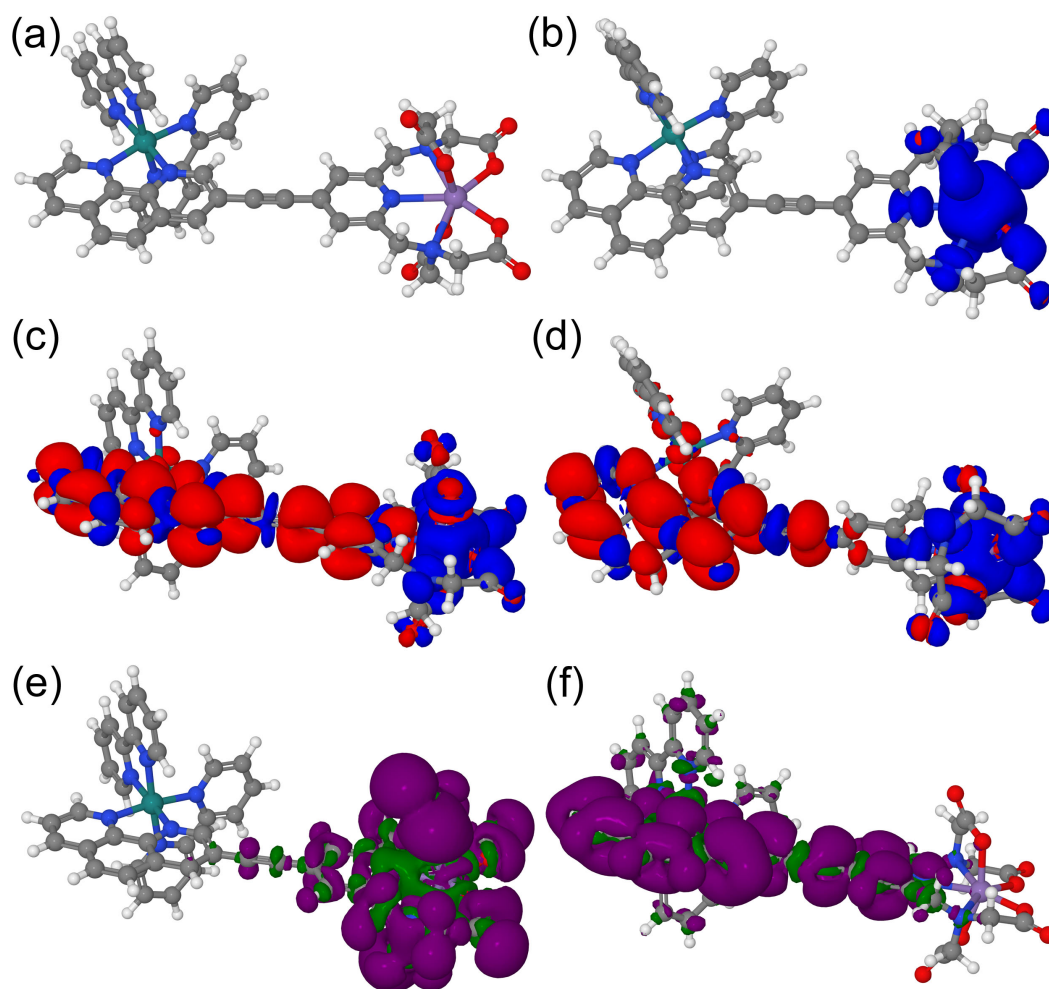


Fig. 7. Results of computational studies on $\text{Ru}\bullet\text{Mn}$. (a) Optimized structure for $\text{Ru}\bullet\text{Mn}$ in its sextet ground state. (b) Spin density for $\text{Ru}\bullet\text{Mn}$ in its ground state sextet state (isosurface at density = 0.0004; blue = α -spin, red = β -spin). (c) Spin density for $\text{Ru}\bullet\text{Mn}$ in its lowest excited quartet state (isosurface at density=0.0004, blue = α -spin, green = β -spin). (d) Spin density for $\text{Ru}\bullet\text{Mn}$ in lowest excited quartet state (isosurface at density = 0.0004, blue = α -spin, red = β -spin) with rotated pyridyl unit at 90° to the phenanthroline unit. (e) Difference density for $\text{Ru}\bullet\text{Mn}$ between neutral and mono-oxidised form (isosurface at density = 0.0004, green = increase, purple = decrease). (f) Difference density for $\text{Ru}\bullet\text{Mn}$ between mono-reduced and neutral form (isosurface at density = 0.0004, green = increase, purple = decrease) with rotated pyridyl unit at 90° to the phenanthroline unit.

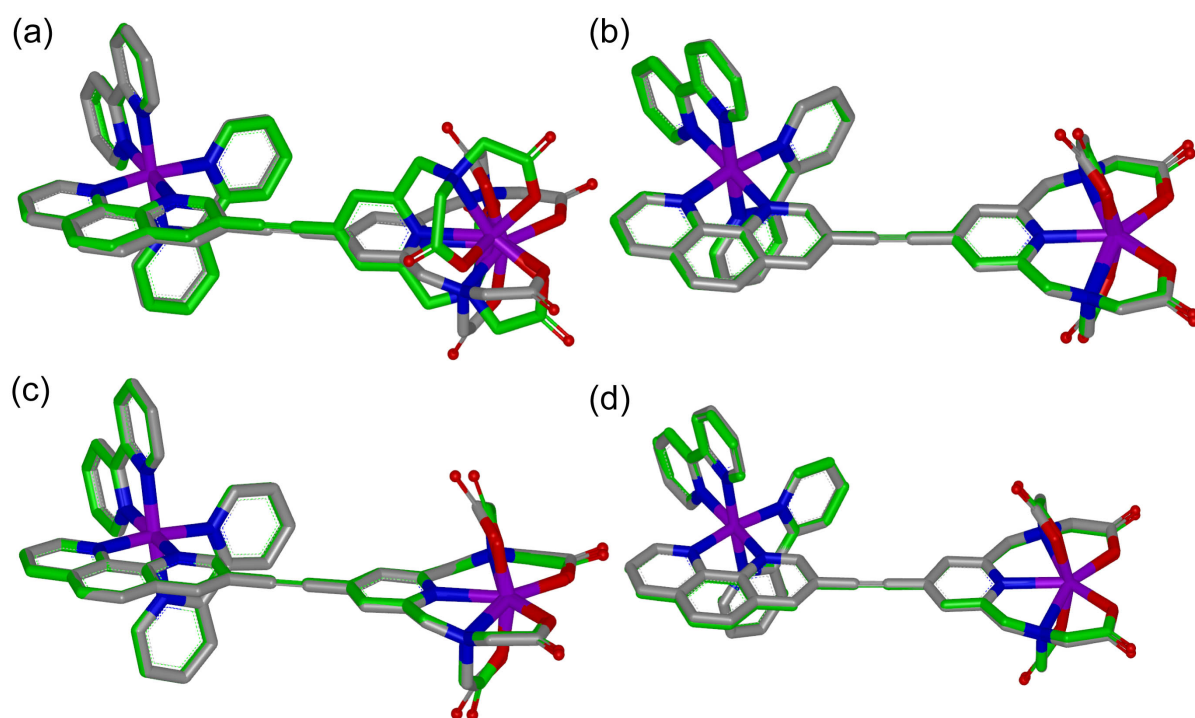


Fig. 8 Overlays of the neutral form of **Ru•Mn** with other forms accessed in the computational experiments. In all panels, the neutral form of **Ru•Mn** is shown in the majority grey colour, the other form being compared to is shown in green. (a) Overlay of **Ru•Mn** in its 'planar' form, with the 'perpendicular' form arising from twisting the pyridyl group with respect to the phen group. (b) Overlay of **Ru•Mn** (⁶A ground state) with **Ru•Mn** (⁴A excited state): the significant change in geometry around the Mn centre indicates its transient oxidation to Mn(III). (c) Overlay of **[Ru•Mn]⁰** (⁶A) with **[Ru•Mn]⁺** (⁵A): the significant change in geometry around the Mn centre indicates its oxidation to Mn(III). (d) Overlay of **[Ru•Mn]⁰** (⁶A) with **[Ru•Mn]⁻** (⁵A): the lack of significant changes in coordination geometry around either metal ion is consistent with a phen-based reduction.

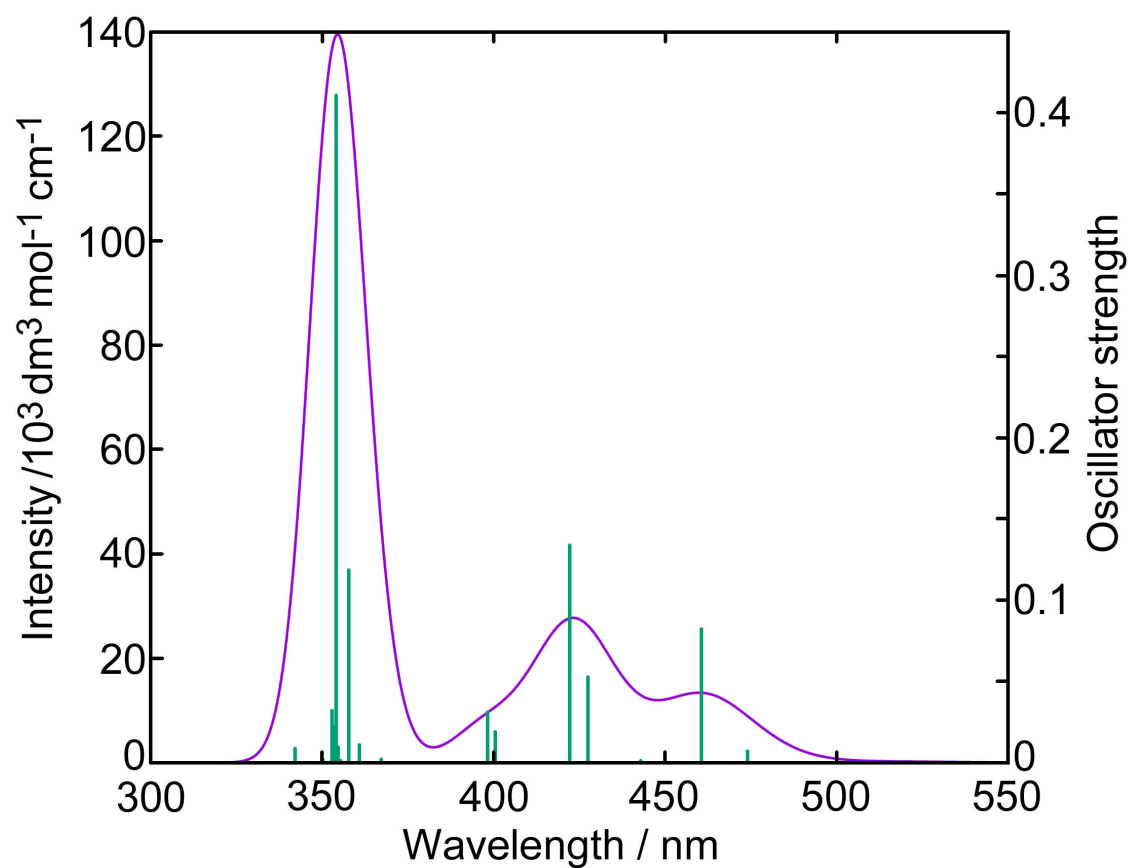


Fig. 9 Simulated UV-VIS spectrum for **Ru•Mn**. The stick spectrum (green lines) indicates the transitions as calculated by TD-DFT with their calculated oscillator strengths. The simulated full spectrum is generated using Gaussian shapes with a FWHM of 1500 cm^{-1} ; this may be compared with the real spectrum in SI.

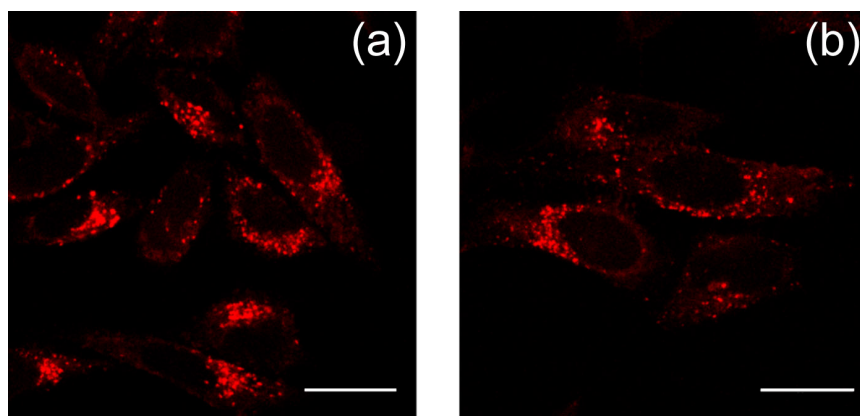
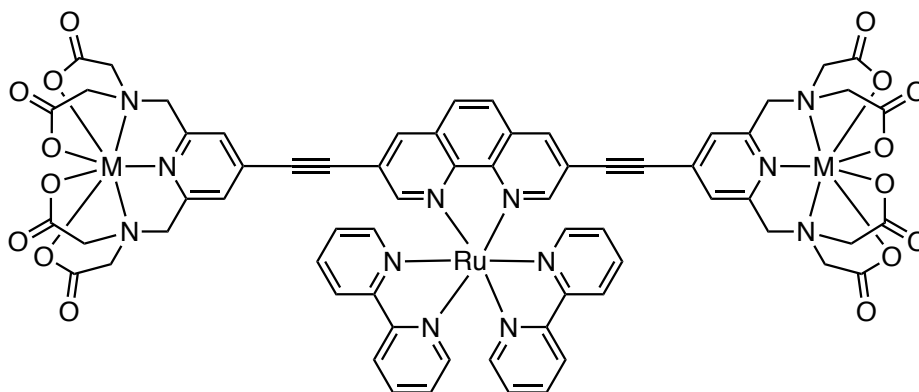


Fig. 10. Confocal microscopy images of HeLa cells incubated with (a) **Ru•Gd** or (b) **Ru•Gd₂** (50 μ M, 4h incubation in each case). $\lambda_{\text{exc}} = 405$ nm; $\lambda_{\text{em}} = 570 - 620$ nm. Scale bars = 20 μ m.

Heteronuclear d-d and d-f Ru(II)/M complexes [M = Gd(III), Yb(III), Nd(III), Zn(II) or Mn(II)] of ligands combining phenanthroline and aminocarboxylate binding sites: combined relaxivity, cell imaging and photophysical studies.

Table of Contents entry



M = Gd(III), Nd(III), Yb(III), Mn(II), Zn(II)

A series of complexes in which a phosphorescent $[\text{Ru}(\text{NN})_3]^{2+}$ core is attached to one or two pendant f-block [Gd(III), Nd(III), Yb(III)] or d-block [Mn(II), Zn(II)] ions have been studied for their relaxivity and cell imaging properties, and photophysical properties which include Ru-to-lanthanide photoinduced energy-transfer and Mn-to-Ru photoinduced electron transfer.